General relativistic simulations of black-hole–neutron-star mergers: Effects of magnetic fields

Zachariah B. Etienne, Yuk Tung Liu, Vasileios Paschalidis, and Stuart L. Shapiro

Phys. Rev. D **85**, 064029 — Published 21 March 2012

DOI: 10.1103/PhysRevD.85.064029

General relativistic simulations of black hole-neutron star mergers: Effects of magnetic fields

Zachariah B. Etienne,[1,*] Yuk Tung Liu,[1] Vasileios Paschalidis,[1] and Stuart L. Shapiro[1,†]

[1]*Department of Physics, University of Illinois at Urbana-Champaign, Urbana, IL 61801*

As a neutron star (NS) is tidally disrupted by a black hole (BH) companion at the end of a BH–NS binary inspiral, its magnetic fields will be stretched and amplified. If sufficiently strong, these magnetic fields may impact the gravitational waveforms, merger evolution and mass of the remnant disk. Formation of highly-collimated magnetic field lines in the disk+spinning BH remnant may launch relativistic jets, providing the engine for a short-hard GRB. We analyze this scenario through fully general relativistic, magnetohydrodynamic (GRMHD) BHNS simulations from inspiral through merger and disk formation. Different initial magnetic field configurations and strengths are chosen for the NS interior for both nonspinning and moderately spinning ($a_{\rm BH}/M_{\rm BH}$=0.75) BHs aligned with the orbital angular momentum. Only strong interior ($B_{\rm max} \sim 10^{17}$G) initial magnetic fields in the NS significantly influence merger dynamics, enhancing the remnant disk mass by 100% and 40% in the nonspinning and spinning BH cases, respectively. However, detecting the imprint of even a strong magnetic field may be challenging for Advanced LIGO. Though there is no evidence of mass outflows or magnetic field collimation during the preliminary simulations we have performed, higher resolution, coupled with longer disk evolutions and different initial magnetic field configurations, may be required to definitively assess the possibility of BHNS binaries as short-hard GRB progenitors.

PACS numbers: 04.25.D-,04.25.dk,04.30.-w

I. INTRODUCTION

With the first direct detection of gravitational waves (GWs) expected in the next few years, numerical relativity simulations will be crucial for distinguishing different GW sources from one another. Mergers of black hole-neutron star (BHNS) binaries are among the most promising sources of gravitational waves detectable by ground-based laser interferometers like LIGO [1, 2], VIRGO [3, 4], GEO [5], LCGT [6], and AIGO [7], as well as by the proposed space-based LISA-like interferometers [8] and DECIGO [9] and third-generation ground-based detectors such as the Einstein telescope [10, 11]. Analysis of gravitational waveforms from BHNS mergers may spark new insights into the behavior of matter at nuclear densities.

Theoretical models indicate that a neutron star-neutron star (NSNS) [12–19] or BHNS [18, 20–26] binary merger may result in a hot, massive disk around a black hole, whose temperatures and densities could be sufficient to trigger a short-hard gamma-ray burst (SGRB). Indeed, SGRBs have been associated with galaxies with extremely low star formation rates (see [27] and references therein for a review), indicating that the source is likely to involve an evolved population, rather than main sequence stars. The number of detectable BHNS mergers in the observable universe is still an open question, due to uncertainties in population synthesis calculations. The estimated event rate of BHNS mergers observable by an Advanced LIGO detector typically falls in the range $\mathcal{R} \sim 0.2$–$300\ {\rm yr}^{-1}$ [28, 29].

Motivated by the significance of BHNS binaries both as detectable GW sources and SGRB candidates, many simulations of BHNS systems have been performed in past years in a Newtonian or post-Newtonian framework (see, e.g., [30–34]) and in conformally-flat relativistic gravitation [20, 21]. Recently, several groups have performed dynamical simulations of BHNS binary inspirals and mergers in full GR [22–26, 35–47].

Over the past few years, we have studied BHNS mergers beginning with the construction of quasiequilibrium circular orbit initial data [48–52] and following up with full GR dynamical simulations [25, 26]. Our GR simulations, and those by other groups, suggest that for initially nonspinning BHs, the remnant disk mass is substantial for $q \equiv M_{\rm BH}/M_{\rm NS} \lesssim 3$ and tends to increase with decreasing q. For a fixed q, the disk mass also increases for smaller NS compaction and for more rapidly spinning BHs aligned with the orbital angular momentum of the binary. For sufficiently high spins, small mass ratios, and/or lower NS compactions, a substantial disk can form following the merger, favoring BHNS mergers as plausible central engines for SGRBs. However, these simulations have yet to account for magnetic field effects – a crucial component in many SGRB models involving a disk around a spinning BH (see, e.g. [53–55]).

For NS surface field strengths $B \lesssim 10^{16}$G, magnetic fields are unlikely to affect the dynamics of the BHNS inspiral and merger [56]. This was shown to be the case for NSNS binary inspirals in [57–60]. Despite this conclusion, magnetic fields may significantly influence the post-merger dynamics, as the fields are likely to be amplified during and after merger. Magnetic fields could stir turbulence in the remnant disk, resulting in angular

* zetienne@illinois.edu
† Also at Department of Astronomy and NCSA, University of Illinois at Urbana-Champaign, Urbana, IL 61801

momentum transport and accretion onto the BH. They could also lead to matter outflow and jets along the BH remnant spin axis [61], another ingredient required by most SGRB models [53–55].

In this paper, we present a new set of fully relativistic BHNS simulations that probes how magnetic fields influence the dynamics and outcome of the merger using our new adaptive mesh refinement (AMR) GRMHD code [62, 63]. Fixing the BH:NS mass ratio at $q = 3$, we consider the cases where the BH possesses no spin (A cases) and moderate spin $a_{\rm BH}/M_{\rm BH} = 0.75$ aligned with the orbital angular momentum (B cases). Since the *internal* magnetic field strength and configuration in a NS is not known, we vary the strength and geometry of the internal fields to study their effects. We find that for low and moderate field strengths $\lesssim 10^{16}$G, magnetic fields do not significantly alter the inspiral and merger dynamics, which is consistent with the result reported in [42]. Here, by low and moderate magnetic fields we mean those with field strengths small or moderate when compared to the virial value of about 10^{18}G; well below this value the field is dynamically unimportant. However, when the central field strength approaches $\sim 10^{17}$G, corresponding to a magnetic to gas pressure ratio of $\sim 0.5\%$, the merger dynamics and remnant disk mass are affected significantly. Yet even with such strong internal magnetic fields, the emitted GWs are not appreciably different from the unmagnetized case, at least for the preliminary set of models considered here. In the late inspiral and merger phases, tidal deformation and disruption of the NS play key roles in distinguishing GWs from BHNSs and BHBHs.

During merger, most of the magnetized NS matter is captured by the BH. Only when the NS interior is seeded with strong magnetic fields ($B_{\rm max} \sim 10^{17}$G, near the center of the NS) is a significant impact on the dynamics observed, resulting in a disk that has up to twice the rest mass as the corresponding unmagnetized case. In all cases the disk accretion rate onto the BH decreases with time immediately after merger, before settling down to a quasistationary state. Most of the magnetic field lines are tightly wound within the remnant disk, and no evidence of magnetic field collimation around the final spinning BH is observed by the time we terminate our simulations. The remnant disk is hot ($T \sim 1$MeV) and massive ($M_{\rm disk} \sim 0.02 M_\odot$ and $\sim 0.1 M_\odot$ for cases A and B, respectively).

The magnetic fields threading the remnant disk may be amplified and tangled on a longer timescale than we simulate, stirring up MHD turbulence. Based on extrapolation of the accretion rates near the end of our simulations, the lifetime of the disk is roughly $0.3(M_0/1.4M_\odot)$s. While there is no evidence of outflows during these preliminary simulations, longer disk evolutions, higher resolution and different B-field geometries may be required to definitively assess the possibility of BHNS binaries as short-hard GRB progenitors.

The following sections are organized as follows. Sections II and III review the basic equations, including our initial data, gauge conditions, matter evolution equations, and diagnostics, as well as their implementation in our GRMHD code. Section IV presents the results of our magnetized BHNS merger simulations. Finally, we summarize our findings and comment on future directions in Sec. V.

II. BASIC EQUATIONS

This section introduces our notation, summarizes our method, and points out the latest changes to our numerical technique as summarized in [25, 26, 62, 63]. Geometrized units ($G = c = 1$) are adopted, except when stated otherwise. Greek indices denote all four spacetime dimensions (0, 1, 2, and 3), and Latin indices label spatial parts only (1, 2, and 3).

We use the 3+1 formulation of general relativity and decompose the metric into the following form:

$$ds^2 = -\alpha^2 dt^2 + \gamma_{ij}(dx^i + \beta^i dt)(dx^j + \beta^j dt) \ . \qquad (1)$$

The fundamental variables for metric evolution are the spatial three-metric γ_{ij} and extrinsic curvature K_{ij}. We adopt the Baumgarte-Shapiro-Shibata-Nakamura (BSSN) formalism [64, 65] in which the evolution variables are the conformal exponent $\phi \equiv \ln(\gamma)/12$, the conformal 3-metric $\tilde{\gamma}_{ij} = e^{-4\phi}\gamma_{ij}$, three auxiliary functions $\tilde{\Gamma}^i \equiv -\tilde{\gamma}^{ij}{}_{,j}$, the trace of the extrinsic curvature K, and the trace-free part of the conformal extrinsic curvature $\tilde{A}_{ij} \equiv e^{-4\phi}(K_{ij} - \gamma_{ij}K/3)$. Here, $\gamma = \det(\gamma_{ij})$. The full spacetime metric $g_{\mu\nu}$ is related to the three-metric $\gamma_{\mu\nu}$ by $\gamma_{\mu\nu} = g_{\mu\nu} + n_\mu n_\nu$, where the future-directed, timelike unit vector n^μ normal to the time slice can be written in terms of the lapse α and shift β^i as $n^\mu = \alpha^{-1}(1, -\beta^i)$. Evolution equations for these BSSN variables are given by Eqs. (9)–(13) in [25]. We adopt standard puncture gauge conditions: an advective "1+log" slicing condition for the lapse and a "Γ-freezing" condition for the shift [66]. The evolution equations for α and β^i are given by Eqs. (2)–(4) in [26], with the η parameter set to $2.2/M$ for the initially nonspinning BH cases and $3.3/M$ for the spinning BH cases, where M is the ADM mass of the BHNS binary. We add a fifth-order Kreiss-Oliger dissipation term to all evolved BSSN, lapse and shift variables to reduce high-frequency numerical noise associated with AMR refinement interfaces (see [67] for a review and references).

The fundamental MHD variables are the rest-mass density ρ_0, specific internal energy ϵ, pressure P, four-velocity u^μ, and magnetic field $B^\mu = n_\nu F^{*\nu\mu}$. Here $F^{*\mu\nu}$ is the dual of the Faraday tensor $F^{\mu\nu}$. Note that B^μ is purely spatial ($B^0 = -n_\mu B^\mu/\alpha = 0$). We adopt a Γ-law equation of state (EOS) $P = (\Gamma - 1)\rho_0\epsilon$ with $\Gamma = 2$, which reduces to an $n = 1$ polytropic law for the initial (cold) neutron star matter. The stress-energy tensor is given by

$$T_{\mu\nu} = (\rho_0 h + b^2) u_\mu u_\nu + \left(P + \frac{b^2}{2}\right) g_{\mu\nu} - b_\mu b_\nu \ , \quad (2)$$

where $h = 1 + \epsilon + P/\rho_0$ is the specific enthalpy and

$$b_\mu = -\frac{P_{\mu\nu} B^\nu}{\sqrt{4\pi}\, n_\nu u^\nu} \quad (3)$$

is the magnetic field measured in fluid's comoving frame, modulo a factor of $1/\sqrt{4\pi}$. Here $P_{\mu\nu} = g_{\mu\nu} + u_\mu u_\nu$ and $b^2 = b^\mu b_\mu$. The comoving magnetic energy density is $u_\mu u_\nu T^{\mu\nu}_{EM} = b^2/2$, where $T^{\mu\nu}_{\rm EM} = b^2 u^\mu u^\nu + (b^2/2) g^{\mu\nu} - b^\mu b^\nu$ is the stress-energy tensor associated with the magnetic field. In the ideal MHD limit, in which the plasma is assumed to have perfect conductivity, the Faraday tensor can be written as $F^{\mu\nu} = \sqrt{4\pi}\, u_\gamma \epsilon^{\gamma\mu\nu\delta} b_\delta$.

In the standard numerical implementation of the MHD equations using a conservative scheme, it is useful to introduce the "conservative" variables ρ_*, $\tilde{S}_i$, $\tilde{\tau}$ and $\tilde{B}^i$. They are defined as

$$\rho_* \equiv -\sqrt{\gamma}\, \rho_0 n_\mu u^\mu \ , \quad (4)$$
$$\tilde{S}_i \equiv -\sqrt{\gamma}\, T_{\mu\nu} n^\mu \gamma^\nu{}_i \ , \quad (5)$$
$$\tilde{\tau} \equiv \sqrt{\gamma}\, T_{\mu\nu} n^\mu n^\nu - \rho_* \ , \quad (6)$$
$$\tilde{B}^i \equiv \sqrt{\gamma}\, B^i . \quad (7)$$

The evolution equations for ρ_*, $\tilde{S}_i$ and $\tilde{\tau}$ can be derived from the conservation of rest mass $\nabla_\mu(\rho_* u^\mu) = 0$ and the conservation of energy-momentum $\nabla_\mu T^{\mu\nu} = 0$, giving rise to Eqs. (27)–(30) in [62].

In the ideal MHD limit, the Maxwell equation $\nabla_\nu F^{*\mu\nu} = 0$ yields the magnetic constraint $\partial_j \tilde{B}^j = 0$ and induction equation $\partial_t \tilde{B}^i + \partial_j (v^j \tilde{B}^i - v^i \tilde{B}^j) = 0$. As shown in [68] and [62], these equations can be rewritten by introducing the electromagnetic 4-vector potential $\mathcal{A}_\mu = \Phi n_\mu + A_\mu$, with $n^\mu A_\mu = 0$. The magnetic constraint and induction equations become

$$B^i = \epsilon^{ijk} \partial_j A_k \ , \quad (8)$$
$$\partial_t A_i = \epsilon_{ijk} v^j B^k - \partial_i (\alpha\Phi - \beta^j A_j) \ , \quad (9)$$

where $\epsilon^{ijk} = n_\mu \epsilon^{\mu ijk}$ is the 3-dimensional Levi-Civita tensor. In [62], we evolve the vector potential and choose the algebraic EM gauge $\Phi = \beta^j A_j/\alpha = -n^j A_j$. We have found that for BHNS simulations, we can achieve better numerical results by imposing the Lorenz gauge $\nabla_\mu \mathcal{A}^\mu = 0$, which gives the evolution equation

$$\partial_t(\sqrt{\gamma}\, \Phi) + \partial_j (\alpha \sqrt{\gamma}\, A^j - \sqrt{\gamma}\, \beta^j \Phi) = 0 \quad (10)$$

for Φ in place of the algebraic gauge condition [63]. Our numerical implementation of Eqs. (8) and (9) guarantees numerically identical B^i (see [62]) regardless of EM gauge in simulations with a uniform-resolution grid. However, interpolations performed on A_i at refinement boundaries on AMR grids will modify A_i, resulting in different B^i near these boundaries. We have shown that in the algebraic gauge $\Phi = -n^j A_j$, there exists a zero-speed mode, which in BHNS simulations manifests itself as a trail of nonzero A_i left behind the orbiting NS [63]. When AMR refinement boxes tracking the motion of the NS cross this "trail", spurious, strong magnetic fields appear on the refinement boundaries. On the other hand, the Lorenz gauge exhibits no zero-speed modes. As a result, the behavior of the B^i fields on refinement boundaries is drastically improved [63]. We therefore adopt the Lorenz gauge for all simulations in this paper.

III. NUMERICAL METHODS

A. Initial data

Our initial data are constructed by solving Einstein's constraint equations in the conformal thin-sandwich (CTS) formalism, which allows us to impose an approximate helical Killing vector by setting the time derivatives of the conformally related metric $\tilde{\gamma}_{ij}$ to zero in the frame corotating with the binary. We model the NS as an irrotational $n = 1$ polytrope, and impose the black hole equilibrium boundary conditions of Cook and Pfeiffer [69] on the black hole horizon. The CTS initial data correspond to a binary in circular quasiequilibrium with a separation chosen to be outside the tidal disruption radius. Details of this method can be found in [26, 52]. The initial data used in this paper are the same as case A (for an initially nonspinning BH) and case B (for an initial BH spin $J_{\rm BH}/M_{\rm BH}^2 = 0.75$) described in [26].

The initial data are calculated using the `Lorene` spectral methods numerical libraries [70]. The excised BH region is filled with constraint-violating initial data, using the "smooth junk" technique we developed and validated in [71] (see also [72, 73]). In particular, we extrapolate all initial data quantities from the BH exterior into the interior with a 7$^{\rm th}$ order polynomial, using a uniform stencil spacing of $\Delta r \approx 0.3 r_{\rm AH}$.

All of the NSs considered in this paper have a compaction of $\mathcal{C} = M_{\rm NS}/R_{\rm NS} = 0.145$, where $M_{\rm NS}$ is the ADM mass and $R_{\rm NS}$ is the (circumferential) radius of the NS in isolation. Since we model the NS with an $n = 1$ ($\Gamma = 2$) polytropic EOS, the rest mass of the NS, M_0, scales with the polytropic constant κ as $M_0 \propto \kappa^{1/2}$. For a NS with compaction $\mathcal{C} = 0.145$, we find the ADM mass for the isolated NS to be $M_{\rm NS} = 1.30 M_\odot (M_0/1.4 M_\odot)$, with an isotropic radius $R_{\rm iso} = 11.2{\rm km}(M_0/1.4M_\odot)$ and circumferential (Schwarzschild) radius of $R_{\rm NS} = 13.2{\rm km}(M_0/1.4M_\odot)$. The maximum rest-mass density of this NS is $\rho_{0,\rm max} = 9 \times 10^{14}{\rm g\ cm}^{-3}(1.4M_\odot/M_0)^2$.

We add a small, poloidal magnetic field via the vector potential of the form

$$A_i = \left(-\frac{y - y_c}{\varpi_c^2}\delta^x{}_i + \frac{x - x_c}{\varpi_c^2}\delta^y{}_i\right) A_\varphi \quad (11)$$

$$A_\varphi = A_b \varpi_c^2 \max(P - P_{\rm cut}, 0)^{n_b} \quad (12)$$

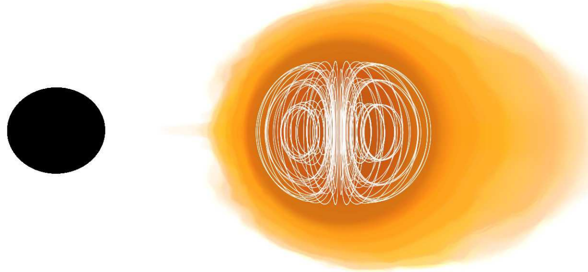

FIG. 1. Magnetic field lines (white) at the time when they are seeded into the NS for case A4. The NS density profile is shown such that darker colors indicate higher densities. The BH apparent horizon is shown in black, and the BH-NS coordinate separation is $6.12M$

where $(x_c, y_c, 0)$ is the coordinate location of the center of mass of the NS, $\varpi_c^2 = (x-x_c)^2 + (y-y_c)^2$, and A_b, n_p and $P_{\rm cut}$ are free parameters. The cutoff pressure parameter $P_{\rm cut}$ confines the B-field inside the neutron star to reside within $P > P_{\rm cut}$. The parameter n_b determines the degree of central condensation of the magnetic field. Similar profiles of initial magnetic fields are also used in numerical simulations of magnetized accretion disks (see, e.g. [74, 75]) and magnetized compact binaries (see, e.g. [42, 76–78]). We set $P_{\rm cut}$ to be 4% of the maximum pressure and n_b=1 or 2. The parameter A_b controls the strength of the initial magnetic field, which can be characterized by the maximum magnetic field inside the NS, as well as the magnetic energy $\mathcal{M}$ defined as

$$\mathcal{M} = \int n_\mu n_\nu T^{\mu\nu}_{\rm EM} dV, \tag{13}$$

where $dV = \psi^6 d^3x$ is the proper volume element on a $t = constant$ spatial slice. $\mathcal{M}$ is the EM energy measured by a normal observer.

Since the magnetic field is expected to remain frozen into the NS during the inspiral phase, we add the fields immediately before tidal disruption to minimize numerical error. Magnetic fields added to the NS at $t = 0$ maintain their original profile within the star for much of the first orbit ($t \lesssim$ milliseconds). Table I summarizes the initial data used in our simulations. Figure 1 shows the magnetic field configuration for one of the cases (A4) at $t = 448.5M$, the time at which the NS is seeded with magnetic fields. The seed magnetic fields are too weak to significantly perturb the quasiequilibrium NS, leading to virtually no change in gravitational field constraint violations.

B. Evolution of the metric and MHD

We evolve the BSSN equations with fourth-order accurate, centered finite-differencing stencils, except on shift advection terms, where we use fourth-order accurate upwind stencils. We apply Sommerfeld outgoing wave boundary conditions to all BSSN fields. Our code is embedded in the Cactus parallelization framework [80], and our fourth-order Runge-Kutta timestepping is managed by the `MoL` (Method of Lines) thorn, with a Courant-Friedrichs-Lewy (CFL) factor set between 0.0625 (in the coarsest refinement level) and 0.5 (in the innermost 4 refinement levels) in all simulations. We decrease the CFL factor in the coarse refinement levels so that we can use a larger value for the parameter η in the shift equation [Eq. (4) in [26]]. We use the Carpet [81] infrastructure to implement the moving-box adaptive mesh refinement. In all AMR simulations presented here, we use second-order temporal prolongation, coupled with fifth-order spatial prolongation. The apparent horizon (AH) of the BH is computed with the `AHFinderDirect` Cactus thorn [82].

The GRMHD equations are evolved by a high-resolution shock-capturing (HRSC) technique [83] that employs PPM [84] coupled to the Harten, Lax, and van Leer (HLL) approximate Riemann solver [85]. The adopted MHD scheme is second-order accurate for smooth flows, and first-order accurate when discontinuities (e.g. shocks) arise. To stabilize our scheme in regions where there is no matter, we maintain a tenuous atmosphere on our grid, with a density floor $\rho_{\rm atm}$ set equal to 10^{-10} times the initial maximum density on our grid. The initial atmospheric pressure $P_{\rm atm}$ is set equal to the cold polytropic value $P_{\rm atm} = \kappa\rho_{\rm atm}^\Gamma$. Throughout the evolution, we impose limits on the atmospheric pressure to prevent spurious heating and negative values of the internal energy ϵ due to numerical errors. Specifically, we require $P_{\rm min} \leq P \leq P_{\rm max}$, where $P_{\rm max} = 10\kappa\rho_0^\Gamma$ and $P_{\rm min} = \kappa\rho_0^\Gamma/2$. Whenever P exceeds $P_{\rm max}$ or drops below $P_{\rm min}$, we reset P to $P_{\rm max}$ or $P_{\rm min}$, respectively. Applying these limits everywhere on our grid would artificially sap the angular momentum in the tidally disrupted NS, allowing matter to fall spuriously into the BH and thereby suppressing disk formation [26]. To effectively eliminate this spurious angular momentum loss, we impose these pressure limits only in regions where the rest-mass density remains very low ($\rho_0 < 100\rho_{\rm atm}$) or deep inside the AH, where $\psi^6 > \psi^6_{\rm thr}$ as in [26]. Here $\psi = e^\phi$ and we set $\psi^6_{\rm thr}$ between 10 and 30.

C. Evolution of magnetic field

We evolve the magnetic induction equation via the 4-vector potential using Eqs. (9) and (10). We stagger the A_i and B^i as in [62]. We store Φ on a staggered grid (i^+, j^+, k^+) [all the other hydrodynamic, BSSN, lapse and shift variables are stored at (i, j, k)], where $i^+ = i + 1/2$ and similarly for j^+ and k^+. We treat the term $-\partial_j(\beta^j\sqrt{\gamma}\Phi)$ in Eq. (10) using a second-order upwind scheme. We evolve Eq. (9) using the finite-volume equations similar to Eqs. (63)–(65) in [62], modified to take into account the second term in Eq. (9), which does not vanish in the Lorenz gauge. The detailed implemen-

TABLE I. Initial data for the BHNS simulations. Here a_{BH}/M_{BH} is the BH spin, Ω is the orbital angular frequency, $B_{\rm max}$ is the maximum value of magnetic field inside the NS, assuming the rest mass of the NS is $1.4M_\odot$; $\mathcal{M}$ is the energy of magnetic field defined in Eq. (13) at the time when B-field is added; W is the gravitational potential energy of the NS in isolation defined in Eq. (65) of [79]. All BHNS systems considered here have the BH:NS mass ratio of 3:1.

Case	a_{BH}/M_{BH}	$M\Omega$	$B_{\rm max}$ (G)	$\mathcal{M}/\lvert W\rvert$	P_c	n_b	Time B is added
A0	0.0	0.0330	0	0	–	–	–
A1			1.3×10^{16}	3.1×10^{-6}	0.04	2	$448.5M$
A2			1.3×10^{16}	1.1×10^{-5}	0.04	1	
A3			1.4×10^{16}	1.2×10^{-5}	0.001	1	
A4			9.7×10^{16}	5.9×10^{-4}	0.001	1	
B0	0.75	0.0328	0	0	–	–	–
B1a			1.3×10^{16}	3.1×10^{-6}	0.04	2	$633.6M$
B1b			1.2×10^{16}	2.9×10^{-6}	0.04	2	$752.8M$
B2			1.3×10^{16}	1.1×10^{-5}	0.04	1	
B3			1.4×10^{16}	1.2×10^{-5}	0.001	1	
B4			9.7×10^{16}	5.9×10^{-4}	0.001	1	

tation is described in [63].

The particular staggering of the A_i and Φ variables coupled with the particular implementation of the HRSC scheme are designed to ensure that the resulting B field obtained by taking the curl operator on A_i [Eqs. (60)–(62) in [62]] is numerically identical to the standard constrained transport scheme based on a staggered algorithm [86]. We have carefully designed an algorithm for the extra term in Eq. (9) so that the additional terms in the A_i evolution equations cancel exactly after taking the curl operator. The resulting numerical values of B^i are thus gauge-invariant in unigrid simulations. We have confirmed numerically that this is indeed the case. However, in simulations with an AMR grid, since we perform interpolations on A_i between refinement levels, values of A_i are not the same in different EM gauges at the refinement boundaries. The resulting B field at the refinement boundaries is also different in general but should converge to a unique, true solution with increasing resolution in any gauge.

As in other numerical relativity simulations, some gauges are better behaved than others. We have demonstrated in [63] that the Lorenz gauge is superior to the algebraic gauge in magnetized BHNS simulations. We therefore adopt the Lorenz gauge in all of the magnetized BHNS simulations presented here.

D. Recovery of primitive variables

At each timestep, we need to recover the "primitive variables" ρ_0, P, and v^i from the "conservative" variables ρ_*, $\tilde\tau$, and $\tilde S_i$. We perform the inversion by numerically solving two nonlinear equations via the Newton-Raphson method as described in [87], using the code developed by Noble et al [88].

Sometimes the "conservative" variables may assume values which are out of physical range, resulting in unphysical primitive variables after inversion (e.g. negative pressure or even complex solutions). This usually happens in the low-density "atmosphere" or deep inside the BH interior where high-accuracy evolution is difficult to maintain. Various techniques have been suggested to handle the inversion failure (see, e.g. [89]). Our approach is mainly to impose constraints on the conservative variables to reduce the inversion failure.

One reason for the inversion failure comes from γ_{ij} losing positive-definiteness during the BSSN evolution due to numerical inaccuracy, which occurs only near the "puncture" deep inside the BH. Before performing the inversion, we check if γ_{ij} is positive-definite by finding its eigenvalues. If γ_{ij} is not positive definite, we reset $\gamma_{ij}\to\psi^4 f_{ij}$ during the inversion, where f_{ij} is the 3D flat metric tensor.

In the absence of magnetic fields, the inversion failure can be avoided completely by enforcing the constraints (see [25] and Appendix A)

$$\tilde S^2 \equiv \gamma^{ij}\tilde S_i\tilde S_j \le \tilde\tau(\tilde\tau+2\rho_*), \text{and} \tag{14}$$

$$\tilde\tau \ge 0 \ , \tag{15}$$

which are the necessary and sufficient conditions for the inversion to produce the primitive variables in the physical range for the Γ-law EOS with $1<\Gamma\le 2$ (see Appendix A). We enforce these constraints in regions where there are no magnetic fields. When the second condition is not met, we reset $\tilde\tau=\tilde\tau_{\rm atm}=10^{-10}\tilde\tau_{0\rm max}$, where $\tilde\tau_{0\rm max}$ is the maximum value of $\tilde\tau$ initially. When the first condition is violated we rescale $\tilde S_i$ so that its new magnitude is $\tilde S^2=\tilde\tau(\tilde\tau+2\rho_*)$.

In the presence of magnetic fields, no simple analogous formulae are available. However, one can prove that (see Appendix A)

$$\tilde\tau \ge \psi^{-6}\frac{\tilde B^2}{8\pi} \tag{16}$$

for any value of primitive variables in the physical range. We therefore impose inequality (16) everywhere: if it is violated, we reset $\tilde{\tau} = \tilde{\tau}_{\rm atm} + \psi^{-6}\tilde{B}^2/8\pi$. However, this does not guarantee that the inversion always produce physically acceptable primitive variables. If failures occur outside the BH after imposing (16), we apply a fix, which consists of replacing the energy equation (6) by the cold EOS, $P = P_{\rm cold}(\rho_0) = \kappa\rho_0^\Gamma$ when solving the system of equations, where κ is the polytropic constant. One can show that this procedure always produces physically valid primitive variables (see Sec. A 4). However, we find that this fix gives rise to discontinuous data deep inside the BH and these data will eventually propagate out of the BH horizon. Note that the success of the "smooth junk" technique [71] requires that the constraint violating initial data filling the interior of the BH horizon be *smooth*. If discontinuous data are used, then information can leak out of the BH horizon. To avoid information leakage outside the BH, we apply the following conditions deep inside the BH:

$$\tilde{\tau} - \frac{\psi^6}{2}\bar{B}^2 - \frac{\bar{B}^2\tilde{S}^2 - (\bar{B}^i\tilde{S}_i)^2}{2\psi^6(W_m + \bar{B}^2)^2} \equiv \tilde{\tau}_m \geq 0, \tag{17}$$

and

$$\tilde{\tau}_m(\tilde{\tau}_m + 2\rho_*) \geq \tilde{S}^2, \tag{18}$$

where $\bar{B}^i = B^i/\sqrt{4\pi}$, $\bar{B}^2 = \gamma_{ij}\bar{B}^i\bar{B}^j$, and W_m satisfies the quartic equation

$$(\psi^{12}W_m^2 - \rho_*^2)(W_m + \bar{B}^2)^2 - W_m^2\tilde{S}^2 - (\bar{B}^i\tilde{S}_i)^2(\bar{B}^2 + 2W_m) = 0.$$

It can be shown that the inequalities (17) and (18) are *sufficient* (but not necessary) conditions for the inversion to yield physically valid primitive variables (see Appendix A). We therefore only use them deep inside the BH where $\psi^6 > \psi^6_{\rm thr}$. We choose the parameter $\psi^6_{\rm thr}$ between 10 and 30. Since the inequalities (17) and (18) are sufficient but not necessary conditions, we do not impose them strictly, but adopt the procedures described at the end of Sec. A 2. We find that this technique gives rise to smoother data in the BH interior preventing contraint-violating information from leaking out of the BH horizon.

E. Diagnostics

During the evolution, we monitor the Hamiltonian and momentum constraints calculated by Eqs. (40)–(43) of [25]. We also monitor the interior mass $M_{\rm int}$ and (z-component of) the interior angular momentum $J_{\rm int}$ of the system contained in the simulation domain. These quantities are defined as integrals over the surface of the outer boundary ∂V) of the computational domain:

$$M_{\rm int} = \frac{1}{2\pi}\oint_{\partial V}\left(\frac{1}{8}\tilde{\Gamma}^i - \tilde{\gamma}^{ij}\partial_j\psi\right)d\Sigma_i, \tag{19}$$

$$J_{\rm int} = \frac{1}{8\pi}\tilde{\epsilon}^k_{zj}\oint_{\partial V} x^j(K^m_k - \delta^m_k K)d\Sigma_m, \tag{20}$$

where $\tilde{\epsilon}_{ijk}$ is the flat-space Levi-Civita tensor. As pointed out in [26], the integrals can be evaluated more accurately by alternative expressions via Gauss's law [67]:

$$\begin{aligned} M_{\rm int} = &\int_V d^3x\left(\psi^5\rho + \frac{1}{16\pi}\psi^5\tilde{A}_{ij}\tilde{A}^{ij} - \frac{1}{16\pi}\tilde{\Gamma}^{ijk}\tilde{\Gamma}_{jik}\right. \\ &\left. + \frac{1-\psi}{16\pi}\tilde{R} - \frac{1}{24\pi}\psi^5K^2\right) \\ &+ \frac{1}{2\pi}\oint_S\left(\frac{1}{8}\tilde{\Gamma}^i - \tilde{\gamma}^{ij}\partial_j\psi\right)d\Sigma_i\ , \end{aligned} \tag{21}$$

$$\begin{aligned} J_{\rm int} = &\frac{1}{8\pi}\tilde{\epsilon}_{zj}{}^n\int_V d^3x\psi^6(\tilde{A}^j{}_n + \frac{2}{3}x^j\partial_n K \\ &- \frac{1}{2}x^j\tilde{A}_{km}\partial_n\tilde{\gamma}^{km} + 8\pi x^j\tilde{S}_n) \\ &+ \frac{1}{8\pi}\tilde{\epsilon}_{zj}{}^n\oint_S \psi^6 x^j\tilde{A}^m{}_n d\Sigma_m\ , \end{aligned} \tag{22}$$

where S is a surface surrounding the BH horizon, V is the volume between S and the outer boundary, $\rho = n_\mu n_\nu T^{\mu\nu}$, and $\tilde{R}$ is the Ricci scalar associated with the conformal 3-metric $\tilde{\gamma}_{ij}$. If our outer boundary were extended to spatial infinity, these integrals would yield the ADM mass and angular momentum of the system and would be constant in time. While our outer boundary ∂V resides in the nearly Minkowski asymptotic regime, it is at a finite distance from the BHNS system. Thus the integrals are only approximately equal to the ADM M and J at $t = 0$ and decreases with time, due to GWs carrying away energy and angular momentum through ∂V.

When hydrodynamic matter is evolved on a fixed uniform grid, our hydrodynamic scheme guarantees that the rest mass M_0 is conserved to machine roundoff error. This strict conservation is no longer maintained in an AMR grid, where spatial and temporal prolongation is performed at the refinement boundaries. Hence we also monitor the rest mass

$$M_0 = \int \rho_* d^3x \tag{23}$$

during the evolution. Rest-mass conservation is also violated whenever ρ_0 is reset to the atmosphere value. This usually happens only in the very low-density atmosphere or deep inside the AH where high accuracy is difficult to maintain.

We measure the thermal energy generated by shocks via the entropy parameter $K \equiv P/P_{\rm cold}$, where $P_{\rm cold} = \kappa\rho_0^\Gamma$ is the pressure associated with the cold EOS. The specific internal energy can be decomposed into a cold part and a thermal part: $\epsilon = \epsilon_{\rm cold} + \epsilon_{\rm th}$ with

$$\epsilon_{\rm cold} = -\int P_{\rm cold} d(1/\rho_0) = \frac{\kappa}{\Gamma - 1}\rho_0^{\Gamma-1}\ . \tag{24}$$

Hence the relationship between K and $\epsilon_{\rm th}$ is

$$\begin{aligned} \epsilon_{\rm th} = \epsilon - \epsilon_{\rm cold} &= \frac{1}{\Gamma-1}\frac{P}{\rho_0} - \frac{\kappa}{\Gamma-1}\rho_0^{\Gamma-1} \\ &= (K-1)\epsilon_{\rm cold}\ . \end{aligned} \tag{25}$$

For shock-heated gas, we always have $K > 1$ (see Appendix B of [26].

Finally, we monitor the mass and spin of the BH during the evolution. They are computed using the isolated and dynamical horizon formalism [90], with the approximate axial Killing vector on the horizon computed as in [91].

F. Gravitational wave extraction

Gravitational waves are extracted using the Newman-Penrose Weyl scalar ψ_4 at various extraction radii between $50M$ and $130M$. We decompose ψ_4 into $s = -2$ spin-weighted spherical harmonics up to and including $l = 4$ modes. At each extraction radius, the retarded time is computed using the technique described in Sec. IIB of [92] to reduce the near-field effect. The wavetrain h_+ and $h_\times$ for each mode are computed by integrating the corresponding mode of ψ_4 twice with time using the fixed frequency integration technique described in [93].

We compute the radiated energy ΔE_{GW}, z-component of angular momentum ΔJ_{GW} and linear momentum ΔP^i_{GW} using expressions equivalent to Eqs. (33), (39), (40) and (49) of [94]. To check the violation of energy and angular momentum conservation, we monitor the quantities

$$\delta E = [M - M_{\rm int}(t) - \Delta E_{\rm GW}(t)]/M \ , \qquad (26)$$

$$\delta J = [J - J_{\rm int}(t) - \Delta J_{\rm GW}(t)]/J \ , \qquad (27)$$

where J is the ADM angular momentum of the initial binary, $M_{\rm int}(t)$ and $J_{\rm int}(t)$ are the interior mass and angular momentum of the system at time t as calculated by Eqs. (21) and (22).

IV. RESULTS

We have performed magnetized simulations of BHNS binaries with BH:NS mass ratio 3:1 including both initially nonspinning BHs (the "A" cases) and BHs with spin parameter set to 0.75 initially (the "B" cases). Table II specifies the AMR grid structure used in the simulations and Table III summarizes the quantitative results. For readers interested only in a brief summary of the most interesting results, please skip to Sec. V. Detailed simulation results are described below.

A. Magnetic Field Study: Nonspinning Black Hole

Figure 2 shows density contours on the orbital plane at selected times for the unmagnetized, zero BH spin case, A0. Notice that the NS density contours in the top-left plot are nearly unchanged after three orbits (top-center plot), confirming that the initial data are consistent with quasiequilibrium. After about 3.5 orbits the NS tidally disrupts (top-right plot), and about 95% of the NS matter promptly falls into the BH. Matter in the low-density NS outer layers far from the accreting funnel of matter forms a tidal tail that wraps around the black hole and smashes into itself near the BH, generating a large amount of shock heating (bottom-left plot). Meanwhile, accretion slows considerably. After intersecting itself, the inner regions of the tidal tail forms a disk that orbits the BH, while the fluid velocity distribution in the outer tail indicates slow accretion onto the disk (bottom-middle plot). Shortly after disk formation, only about 2% of the NS matter remains outside the BH (bottom-right plot), and the density directly outside the AH begins to plummet, ultimately forming a low-density cavity around the BH similar to the one shown more prominently in the bottom left frame of Fig. 5. This cavity indicates the presence of an innermost stable circular orbit (ISCO).

Figure 3 shows the accretion history for all cases in which the BH has zero spin initially. Regardless of magnetic field configuration or strength, by $t \approx 570M$ about 95% of the NS matter – including the most strongly magnetized matter in the star – has been accreted by the BH. After this violent merger, the only case that noticeably deviates from the magnetic-free case (A0) is case A4, the case in which the initial seed magnetic fields are both strong ($|B|_{\rm max} \sim 10^{17}$G) and pushed to the NS surface ($P_c = 0.001$). The disk mass in case A4 is two times larger than any other case, but the final disk is only about 2.5% of the initial NS rest mass – much smaller than in similar BHNS simulations with a moderate aligned BH spin, in which disk masses of $\sim 10\%$ are common. Case A3 is identical to case A4, except for the fact that its seed magnetic fields are about an order of magnitude weaker ($|B|_{\rm max} \sim 10^{16}$G), and its accretion history is virtually indistinguishable from that of case A0. Thus it is the magnetic field strength – and not the different geometries explored here – that significantly influences the dynamics. The final accretion rate implies a disk half-life of between 3500–5500M or 100–150$(M_0/1.4M_\odot)$ms (depending on what points are chosen to calculate the final slope).

Figure 4 plots magnetic energy outside the AH versus time, for all magnetized nonspinning BH cases studied. Magnetic fields were added shortly before tidal disruption. The magnetic fields do not change significantly in the NS prior to disruption, but at the point of disruption, there are two competing effects that influence the magnetic energy. For one, the NS is being tidally disrupted, stretching the magnetic field lines, amplifying the magnetic field strength and energy. On the other hand, the magnetized fluids comprising the NS are being rapidly accreted into the BH. Our results show that there is a slight amplification of magnetic energy during tidal disruption, but after tidal disruption the magnetic energy is always less than the magnetic energy in the seed magnetic fields. The evolution is followed for $\sim 50(M_0/1.4M_\odot)$ms (assuming NS rest mass of $1.4M_\odot$) after disk formation, but ultimately no large magnetic energy amplification is observed. This is likely due to the fact that the magnetic fields in the disk are mostly toroidal (see Fig. 5) and once

TABLE II. Grid configurations. Here, $N_{\rm AH}$ denotes the number of grid points covering the diameter of the (spherical) AH initially, and $N_{\rm NS}$ denotes the number of grid points covering the smallest diameter of the neutron star initially.

Case	Grid Hierarchy (in units of M)$^{(a)}$	Max. resolution	$N_{\rm AH}$	$N_{\rm NS}$
A0–A4	(196.7, 98.35, 49.18, 24.59, 12.29, 6.147, 3.073, 1.414 [1.660])	$M/32.5$	41	85
B0–B4	(210.2, 92.49, 46.24, 23.12, 11.56, 5.780, 2.890, 1.445 [1.642], 0.7554 [N/A])	$M/60.9$	56	80

$^{(a)}$ There are two sets of nested refinement boxes: one centered on the NS and one on the BH. This column specifies the half side length of the refinement boxes centered on both the BH and NS. When the side length around the NS is different, we specify the NS half side length in square brackets. If there is no corresponding NS refinement box (as is the case when the NS is significantly larger than the BH), we write [N/A] for that box.

TABLE III. Magnetized BHNS simulation results. Here $M_{\rm disk}$ is the rest mass of the material outside the AH at the end of the simulation, $\tilde{a}_{\rm f} = a_{\rm BH}/M_{\rm BH}$ is the spin parameter of the BH at late times determined by the isolated horizon formalism. The total energy and angular momentum carried off by the gravitational radiation are given by $\Delta E_{\rm GW}$ and $\Delta J_{\rm GW}$, respectively. $v_{\rm kick}$ is the kick velocity due to recoil. $N_{\rm orbits}$ specifies the number of orbits in the inspiral phase before merger, defined as the time at which the (2,2) mode of the GW amplitude reaches maximum. δE and δJ measure the violation of energy and angular momentum conservation, as defined in Eqs. (26) and (27), respectively, at the end of the simulation. The error in $v_{\rm kick}$ is estimated by comparing the results obtained by several GW extraction radii between $50M$–$100M$.

Case	$M_{\rm disk}/M_0$	$\tilde{a}_{\rm f}$	$\Delta E_{\rm GW}/M$	$\Delta J_{\rm GW}/J$	$v_{\rm kick}$ (km/s)	$N_{\rm orbits}$	δE	δJ
A0	0.019	0.55	0.011	0.20	40 ± 2	4.8	0.2%	2%
A1	0.017	0.55	0.011	0.20	40 ± 2	4.8	0.2%	2%
A2	0.017	0.55	0.011	0.20	40 ± 2	4.8	0.2%	2%
A3	0.015	0.55	0.011	0.20	40 ± 2	4.8	0.2%	3%
A4	0.028	0.55	0.011	0.20	40 ± 2	4.8	0.1%	1%
B0	0.098	0.84	0.011	0.15	67 ± 6	6.9	0.6%	8%
B1a	0.090	0.84	0.011	0.15	67 ± 6	6.9	0.6%	8%
B1b	0.090	0.84	0.011	0.15	67 ± 6	6.9	0.6%	8%
B2	0.090	0.84	0.011	0.15	67 ± 6	6.9	0.6%	7%
B3	0.090	0.84	0.011	0.15	67 ± 6	6.9	0.6%	7%
B4	0.117	0.85	0.010	0.14	54 ± 4	6.8	0.4%	7%

the disks have formed magnetic winding saturates. Amplification of magnetic fields by instabilities such as the magnetorational instability (MRI) may occur, but the resolution in our simulations may not be high enough to resolve the small-scale turbulence associated with these instabilities.

Notice that the magnetic energy in case A2 is about three times that of A1, both initially and when the simulation was terminated. These cases differ only in the degree of central condensation of the initial magnetic field (see Table I).

Cases A2 and A3 are identical except for the pressure cutoff of the seed magnetic fields. In case A2 magnetic fields are set to zero for pressures $P < P_c = 0.04P_{\rm max}$, where $P_{\rm max}$ is the maximum pressure of the NS. However, in case A3 P_c is set to 0.001, so the seed magnetic fields are pushed much closer to the NS surface. This results in about a 16% amplification of initial magnetic energy in case A3 (Fig. 4), *but increases the final magnetic energy by about a factor of 15.* This is consistent with the fact that the core of the NS is invariably accreted into the BH during merger in these BHNS simulations, so the disk is comprised of what were the outer layers of the NS. Thus, the stronger the seed magnetic field in the outer layers of the NS, the stronger and more dynamically relevant the magnetic fields in the disk.

Cases A3 and A4 differ only in initial seed magnetic field strength; the seed magnetic fields are uniformly about an order of magnitude stronger in case A4. Figure 3 demonstrates that the physical extent of the disk is very strongly influenced by the strong seed magnetic fields of case A4. Figure 4 reinforces that observation; though only about 1% of the NS rest mass exists in the disk of A3, less than 0.5% of the seed magnetic energy remains in the disk. Compare this to case A4, where the disk mass is about twice as large, but where more than an order of magnitude more magnetic energy remains in the disk.

Magnetic fields play an important dynamical role in only one nonspinning case, A4, amplifying the disk mass by a factor of two. Figure 5 shows how the magnetic field configuration evolves in this case, from $t = 448.5M$ when the magnetic fields are first seeded into the NS (top-right), until the simulation is stopped at $t = 2620M$ (bottom-right). Magnetic field lines are greatly stretched during disk formation (third row on the right), result-

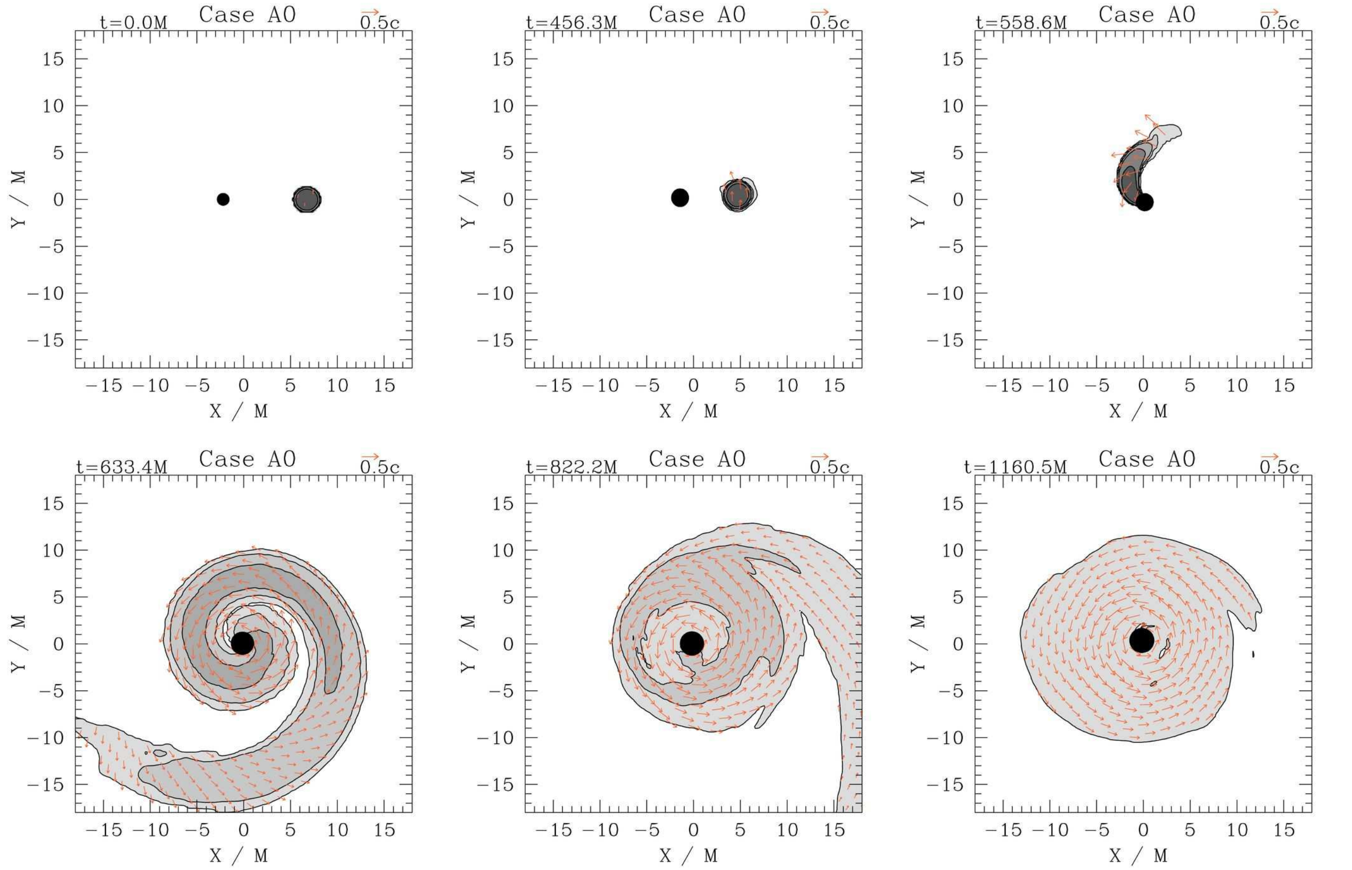

FIG. 2. Orbital-plane rest mass density contours at selected times for case A0. Contours are plotted according to $\rho_0 = \rho_{0,\max}(10^{-0.92j})$, ($j$=0, 1, ... 5), with darker greyscaling for higher density. The maximum initial NS density is $\kappa\rho_{0,\max} = 0.126$, or $\rho_{0,\max} = 9 \times 10^{14}$g cm$^{-3}(1.4M_\odot/M_0)^2$. Arrows represent the velocity field in the orbital plane. The black hole AH interior is marked by a filled black circle. The ADM mass for this case is $M = 2.5 \times 10^{-5}(M_0/1.4M_\odot)s= 7.6(M_0/1.4M_\odot)$km.

ing in a strongly-magnetized disk. At late times, the magnetic fields that remain in the disk are very tightly wound. The bottom left and center frames of the figure show that a cavity has formed around the BH near the end of the simulation. This hollow region is indicative of the presence of an ISCO, which is interesting because it has been suggested that stresses in magnetized disks may suppress the presence of an ISCO [95, 96]. However, it may be that longer simulations are required for the disk cavity to be filled.

The significant boost in disk mass in case A4 indicates that with sufficiently strong NS magnetic fields, merger dynamics may be significantly affected. Figure 6 compares orbital-plane density contours in cases A0 (unmagnetized) and A4 during the late stages of tidal disruption. Notice that the stronger magnetic pressures in case A4 push out the outer layers of the NS during tidal disruption. Nevertheless, Fig. 7 shows that the magnetic pressure in this matter distribution does not exceed 3% the gas pressure at the same time as Fig. 6. Therefore, large changes in remnant disk mass do not require huge magnetic-to-gas pressure ratios.

Figure 8 compares A0 and A4 rest-mass density profiles when these simulations were stopped at $t = 2620M$. The density profiles in these two cases are similar; at the end of the simulation, low-density matter still flows *into* the BH from the poles. For A4, it is clear from the b^2 contour plot (bottom graph) that most of the magnetic fields are confined inside the remnant disk near the equatorial plane, consistent with the magnetic field-line plots in Fig. 5.

Compared to case A0, the final disk in case A4 is more massive, and the accretion rate is lower (Fig. 3). Figure 9 compares the distribution of rest-mass density and entropy ($\log K$) in the remnant disks of cases A0 and A4, at the time shortly after disk formation. The disk in case A0 is of roughly uniform rest-mass density in the orbital plane. Though the disk volume in cases A4 and A0 are comparable, the case A4 disk is about twice as massive as A0. Entropy in case A4 is lower, and entropy contours fall off rapidly with density. On the other hand, the entropy in case A0 is much more uniform in the disk, with only a slight drop near the BH. Thus in the nonspinning case, adding strong seed magnetic fields to the NS results in colder, denser, more massive disks.

Figure 10 shows b^2 profiles for case A4's disk, plot-

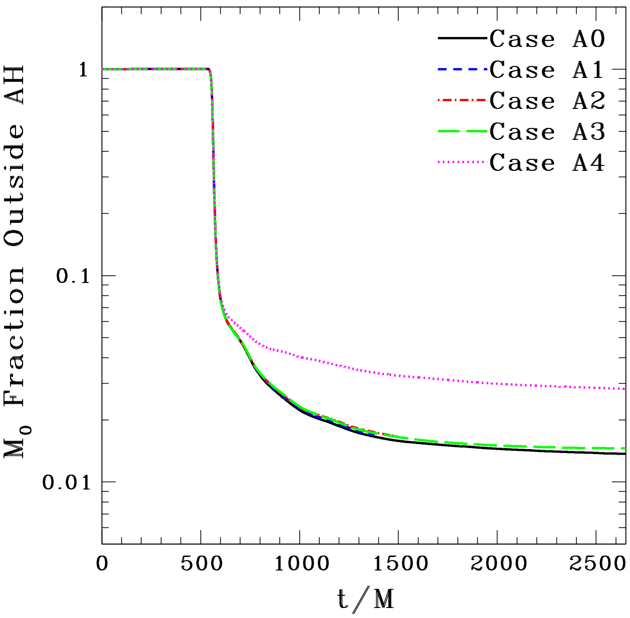

FIG. 3. Rest-mass fraction outside the AH for all cases in which the BH is initially nonspinning.

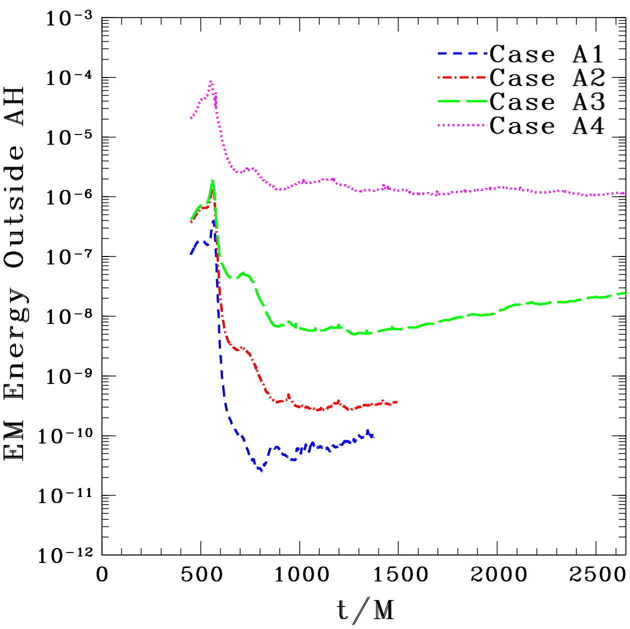

FIG. 4. Total magnetic energy $\mathcal{M}$ outside the AH for all magnetized cases in which the initial BH possesses zero spin, normalized by the ADM mass $M = 9.3\times10^{54}(M_0/1.4M_\odot)$erg.

ted at the same time as in Fig. 9. The strong magnetic fields in A4 enhance the final disk mass by more than a factor of two, even though magnetic pressure never exceeds about 3% of the gas pressure, with typical values around 0.01% (left plot)–about an order of magnitude lower than during tidal disruption (Fig. 7, left frame). Short-wavelength variations in b^2 contours appear near the BH only, with longer-wavelength variations outside. This is likely a numerical artifact, since the disk spans about four AMR refinement levels, which are centered on the BH. Each refinement level drops the resolution by a factor of two, meaning that matter in the outer reaches of this disk is more poorly resolved by a factor of 16 than the region near the BH. This filtering of wavelengths due to AMR likely suppresses magnetic-induced turbulence in the disk.

Figure 11 contrasts $b^2/(2P)$ contours for cases A3 and A4. As $b^2/(2P)$ approaches unity, magnetic fields should have more of a dynamical impact. Case A3 is identical to A4, except its seed magnetic fields are weaker by an order of magnitude. Correspondingly, typical values of $b^2/(2P)$ in this late-time disk are roughly 2–3 orders of magnitude lower in case A3 than A4. This is consistent with the finding that the remnant disk mass and accretion rate are unaffected by magnetic fields in case A3; pressure from the magnetic fields is simply too small to be dynamically relevant. Thus, initial internal magnetic pressures of order 0.1% of gas pressure may be required for magnetic fields to have a significant impact on the system's dynamics.

B. Magnetic Field Study: Spinning Black Hole

Figure 12 outlines the basic evolution scenario for the fiducial $a_{\rm BH}/M_{\rm BH}$=0.75 (henceforth "spinning") case, B0. Unlike the nonspinning case, the NS is slightly distorted from its equilibrium shape after about three orbits (top-left plots, cf. top-left plots in Fig. 2). Although the spinning cases start with the same initial orbital angular frequency as the nonspinning cases, all spinning cases require about two more orbits before an accretion funnel forms (top-right frame). This is due to the well-known "orbital hang-up" effect. Unlike the nonspinning case, in which about 95% of the NS matter immediately funnels into the BH, strong frame-dragging in the spinning cases twists the accreting funnel around the BH, promptly accreting only $\sim$70% of the NS matter. Accretion slows after the funnel twists around the BH and intersects itself, generating shock heating and producing a small, dense disk-like structure that expands and rarefies as it orbits the BH. Notice that this "disk" is much smaller and denser than in the nonspinning cases (bottom-left plot, cf. Fig. 2). Attached to this small "disk", the outer layers of the NS have formed a long tidal tail, which is ejected to a large radius before slowly falling back onto the expanding but accreting "disk" (bottom-middle frame). The disk continues its expansion as much of the tail falls into it. Near the time when the simulation is stopped, we find no indication of a cavity near the BH (bottom-right frame). Longer simulations may be required for a cavity to appear, which might indicate the presence of an ISCO. Note that in contrast with the expected long-term evolution of this unmagnetized case,

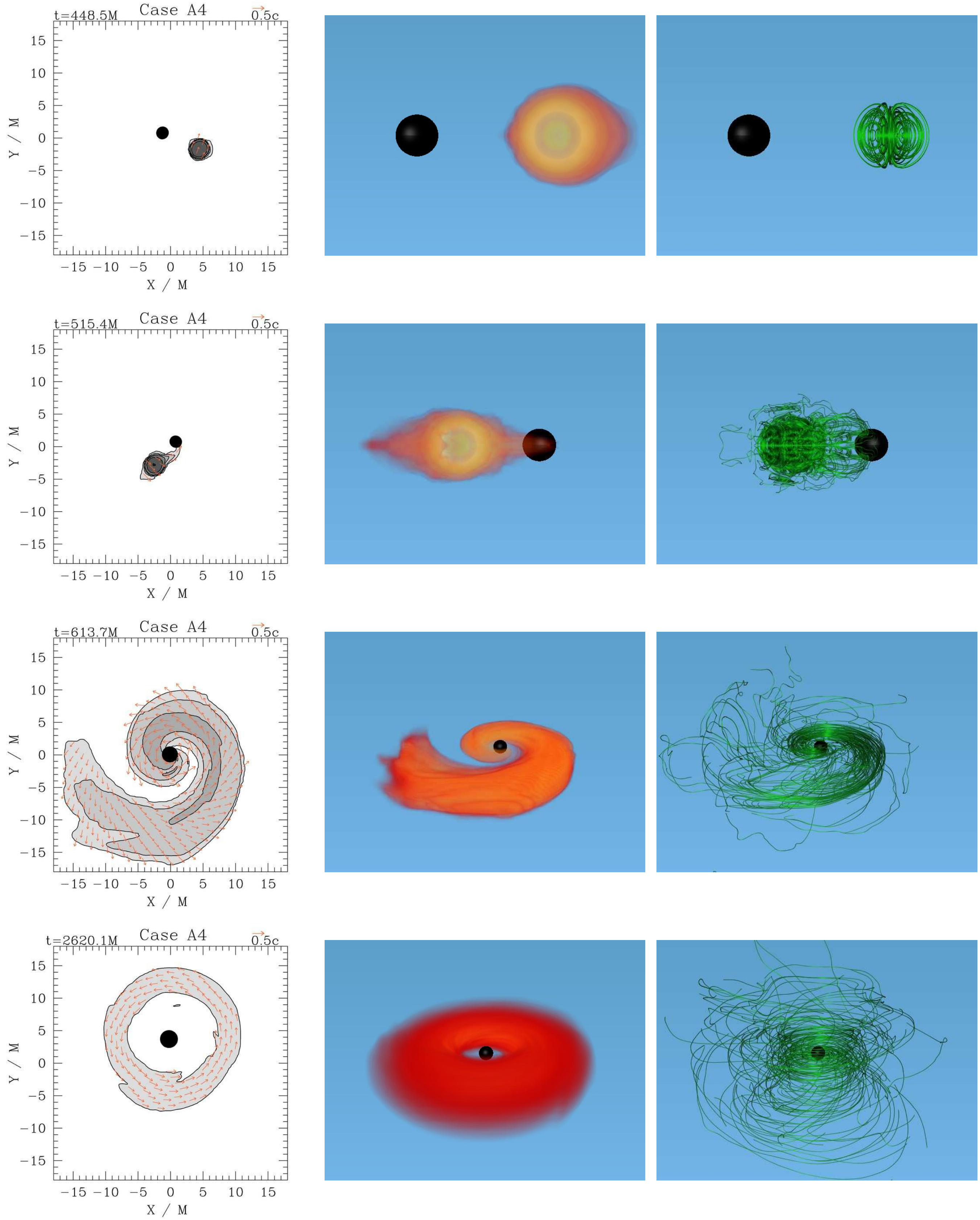

FIG. 5. Orbital-plane rest-mass density contours (left column), 3D density profiles (middle column) and 3D magnetic field lines (right column) at four selected times for case A4. The times in the rows (top to bottom) are t/M =448.5, 515.4, 613.7, and 2620. Density contours in the orbital plane (left column) are plotted according to $\rho_0 = \rho_{0,\rm max}(10^{-0.92j})$, ($j$=0, 1, ... 5), with darker greyscaling for higher density. The maximum initial NS density is $\kappa\rho_{0,\rm max} = 0.126$, or $\rho_{0,\rm max} = 9 \times 10^{14}$g cm$^{-3}(1.4M_{\odot}/M_0)^2$. Arrows in density contour plots represent the velocity field in the orbital plane, and the black hole AH interior is marked by a filled black circle. Magnetic fields are plotted as streamlines of the magnetic field vector B^i, distributed in proportion to $|B^i|$. The ADM mass for this case is $M = 2.5 \times 10^{-5}(M_0/1.4M_{\odot})s= 7.6(M_0/1.4M_{\odot})$km.

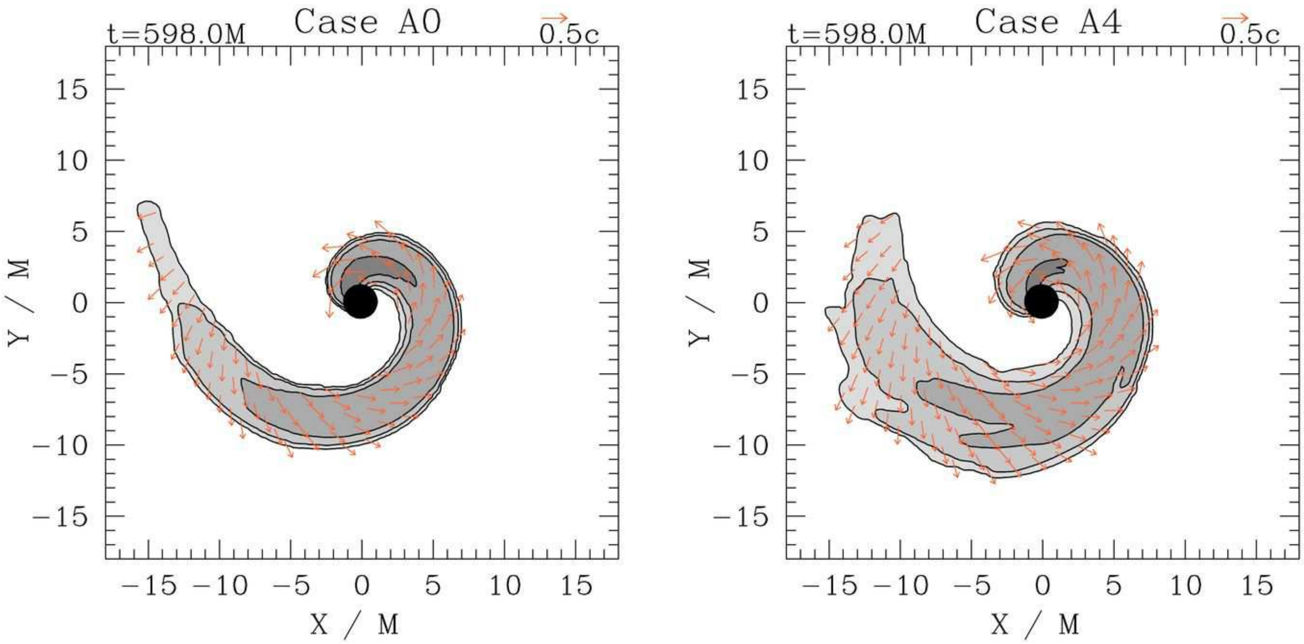

FIG. 6. Rest-mass density and velocity profile snapshots during NS tidal disruption for cases A0 (left) and A4 (right). Density contours are plotted in the orbital plane according to $\rho_0 = \rho_{0,\max}(10^{-0.92j})$, ($j$=0, 1, ... 5), with darker greyscaling for higher density. The maximum initial NS density is $\kappa\rho_{0,\max} = 0.126$, or $\rho_{0,\max} = 9\times10^{14}$g cm$^{-3}(1.4M_\odot/M_0)^2$. Arrows represent the velocity field in the orbital plane, and the black hole AH interior is marked by a filled black circle. The ADM mass for this case is $M = 2.5\times10^{-5}(M_0/1.4M_\odot)$ s= $7.6(M_0/1.4M_\odot)$km.

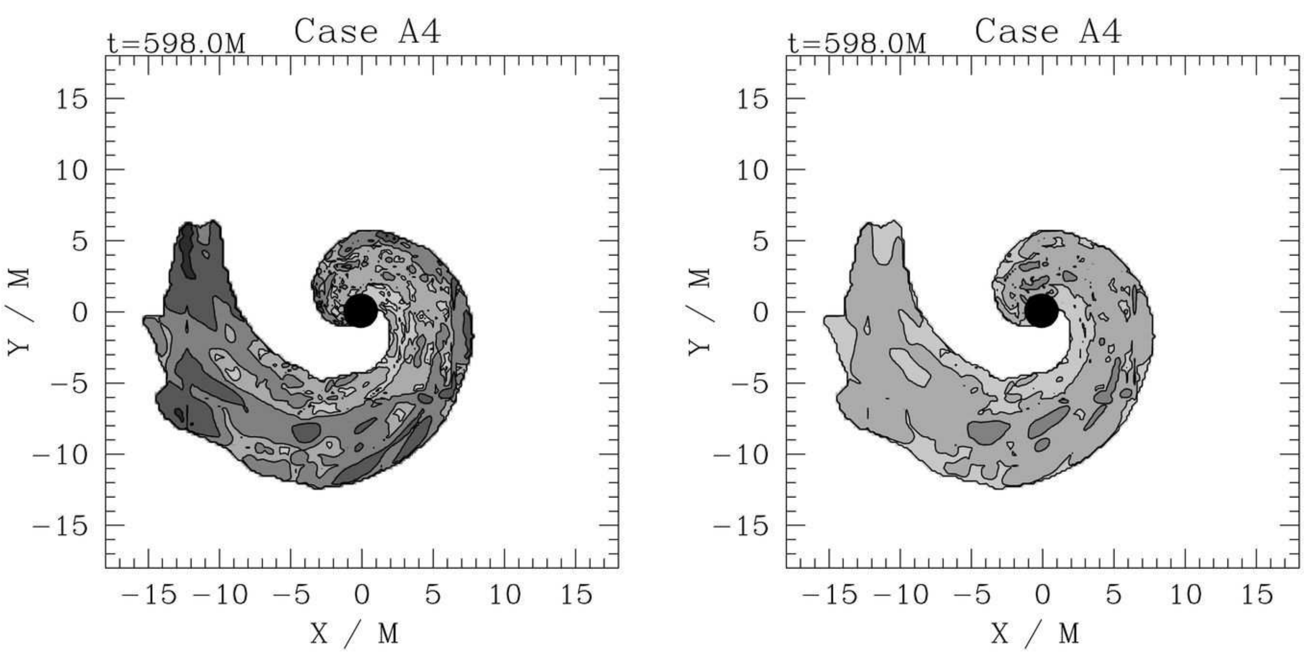

FIG. 7. Pressure ratio $b^2/(2P)$ (left) and magnetic pressure $b^2/2$ (right) contours during NS tidal disruption, at the same time as Fig. 6, plotted according to $b^2/(2P) = 10^{-1.5}(10^{-1.3j})$, ($j$=0, 1, ... 5), and $\kappa b^2 = 10^{-5}(10^{-2.2j})$, ($j$=0, 1, ... 5). Darker greyscaling denotes higher values. Contours are only plotted for regions with densities higher than the lowest-density ρ_0 contours in Fig. 6. In cgs units, $\kappa^{-1} = 6\times10^{36}$dyn cm$^{-2}(1.4M_\odot/M_0)^2$.

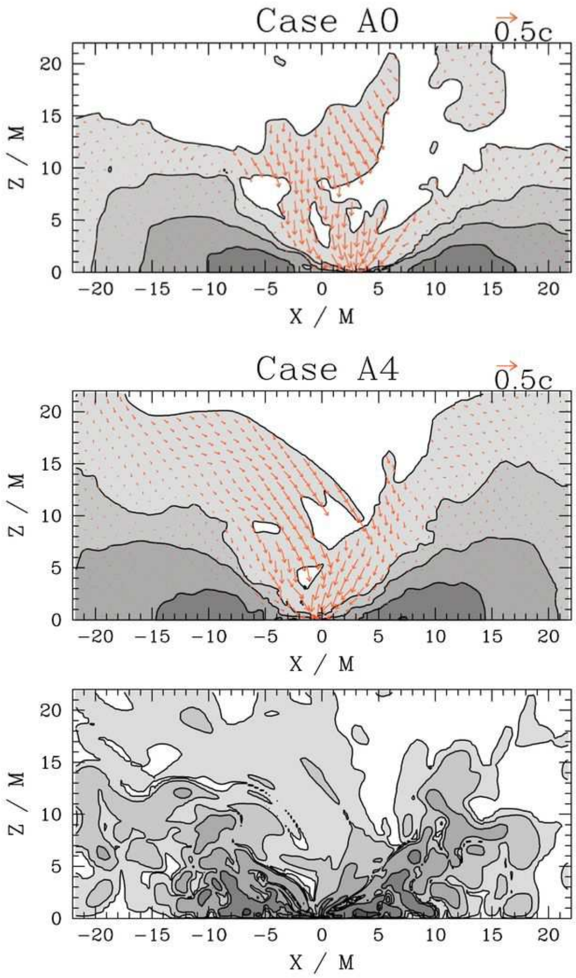

FIG. 8. Rest-mass density contours for case A0 (top), A4 (middle), and magnetic energy density b^2 (bottom) profile for A4 in the meridional plane at the end of simulations ($t = 2620M$). Density contours are plotted according to $\rho_0 = \rho_{0,\max}10^{-7.6+0.717j}$, $(j = 0, ..., 6)$, with darker greyscaling for higher density. b^2 contours are plotted according to $\kappa b^2 = 10^{-12+0.833j}$, $(j = 0, ..., 6)$. The maximum initial NS density is $\kappa\rho_{0,\max} = 0.126$, or $\rho_{0,\max} = 9 \times 10^{14}$g cm$^{-3}(1.4M_\odot/M_0)^2$. Arrows represent the velocity field in the meridional plane. In cgs units, the ADM mass for this case is $M = 2.5 \times 10^{-5}(M_0/1.4M_\odot)$ s$=7.6(M_0/1.4M_\odot)$km, and $\kappa^{-1} = 6 \times 10^{36}$erg cm$^{-3}(1.4M_\odot/M_0)^2 = 7 \times 10^{15}$g cm$^{-3}(1.4M_\odot/M_0)^2$.

stresses in magnetized disks may suppress the formation of hollow regions around the ISCO [95, 96].

The corresponding accretion history for all cases in which the BH initially has spin is shown in Fig. 13. Similar to the nonspinning cases, only the most strongly magnetized case, B4, has an appreciably different accretion history. The NS in case B4 possesses the same magnetic field geometry and strength as the NS in the (nonspinning) case A4: the seed magnetic fields are both strong ($|B|_{\max} \sim 10^{17}$G, initially) and pushed all the way to the NS surface ($P_c = 0.001$). The magnetic fields in case B4 increase the disk mass from about 10% to 14%, a net 40% amplification in disk mass. Notice also that BH spin alone has a *very significant* influence on final disk mass; increasing initial aligned BH spin from zero to $a_{\rm BH}/M_{\rm BH}$=0.75 increases the final disk mass by about an order of magnitude (∼0.9% – ∼10%). Based on the final accretion rate, the half-life of the disk is roughly $5000M$, or $\sim 140(M_0/1.4M_\odot)$ms.

Figure 14 plots the magnetic energy outside the AH versus time for all spinning, magnetized cases. During merger there are two competing effects: magnetic energy will increase as the NS tidally disrupts and the field lines are stretched, while magnetic energy outside the AH will decrease as magnetized NS matter is accreted into the BH. This major accretion event occurs at $t \approx 900M$ for all spinning cases, corresponding to a spike in magnetic energy at that time. At $t = 1000M$, only about 20% of the NS matter remains outside the BH, but the magnetic energy in all cases is *higher* than when the seed fields were added to the NS, indicating that a large amplification in magnetic field strength has occurred. Only case B4 has sufficiently strong magnetic fields to severely impact the disk dynamics; the disk mass is amplified by about 40%, and the magnetic energy in this case is 1–2 orders of magnitude stronger than any other case at all times.

To determine the sensitivity of our results on the time at which the magnetic fields were added to the NS, two simulations were performed: cases B1a and B1b. These simulations are identical except the seed magnetic fields were added to the NS about half an orbit later in case B1b. The accretion histories of cases B1a and B1b overlap completely, implying that the bulk dynamics are unaffected by when the magnetic fields were inserted into the NS. During and directly after the merger ($t \approx 900M$), magnetic energy in cases B1a and B1b overlap. After merger, only a tiny fraction of the fields in the outer layers of the NS remains outside the AH. Correspondingly, the magnetic energy plummets in both cases to negligibly small values, yet agree to within an order of magnitude even at late times. Thus we conclude that the final result is largely insensitive to when the seed magnetic fields were added.

Next we analyze how magnetic fields evolve over time in case B4, starting with the time at which they were seeded into the NS (top-right frame of Fig. 15). At the onset of tidal disruption (second row), the magnetic field structure has changed significantly, even within the nondisrupted regions of the NS. Apparently the magnetic fields have undergone some slight rearrangement since they were added to the NS.

After the accretion funnel has wrapped around the BH and intersected itself, it forms a small disk-like structure around the BH (bottom frames). In this "disk" region, the magnetic fields wind around the BH. The B4 simulation is continued for about $30(M_0/1.4M_\odot)$ms after tidal disruption, and then it is stopped. At this time, the BH+disk system has drifted significantly (bottom plots of 15), due to gauge effects and the gravitational-

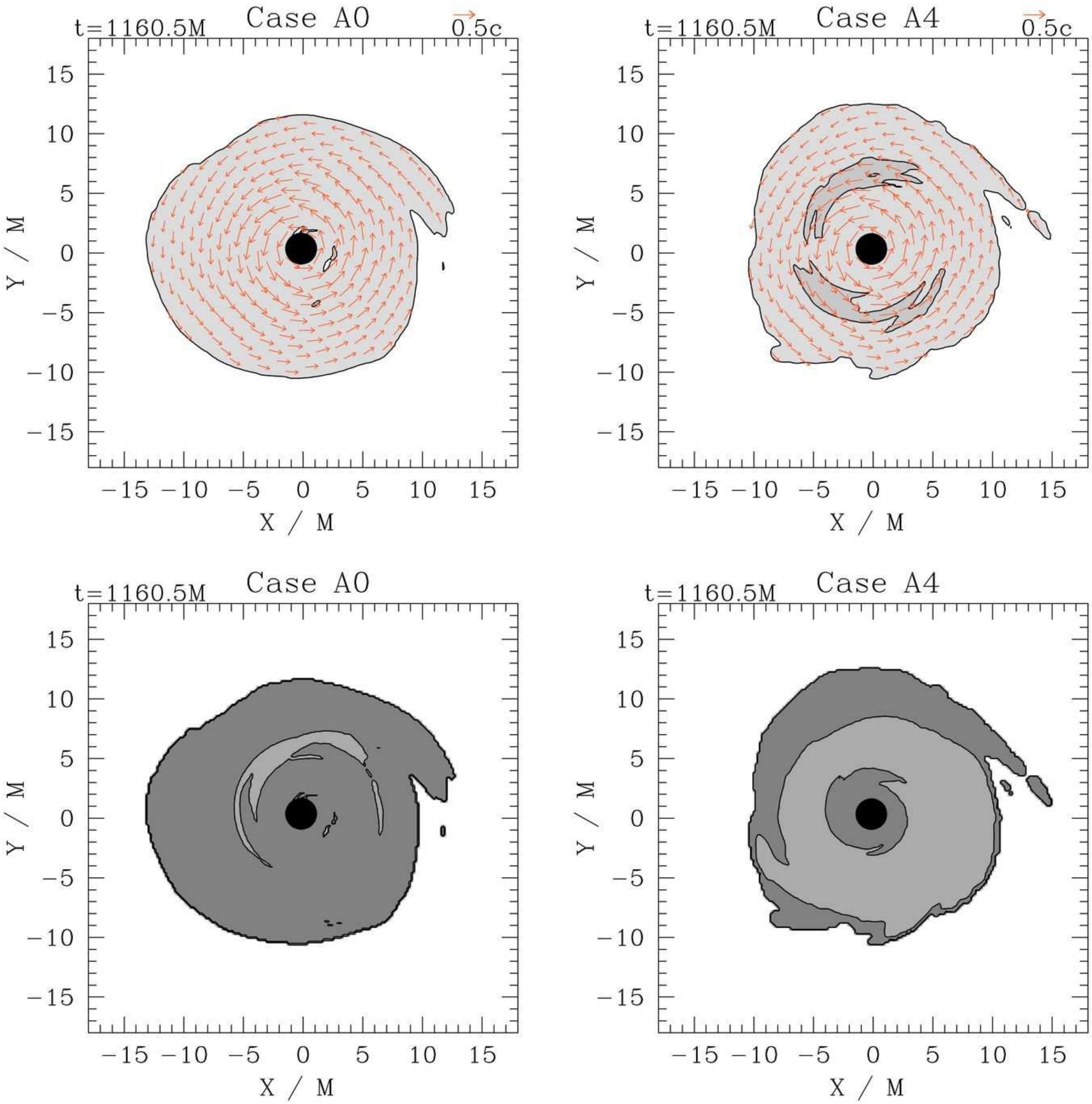

FIG. 9. Top two plots: Rest-mass density and velocity snapshots shortly after disk formation for cases A0 (left) and A4 (right). Density contours are plotted in the orbital plane according to $\rho_0 = \rho_{0,\max}(10^{-0.92j})$, ($j$=0, 1, ... 5), with darker greyscaling for higher density. The maximum initial NS density is $\kappa\rho_{0,\max} = 0.126$, or $\rho_{0,\max} = 9 \times 10^{14}\mathrm{g\ cm}^{-3}(1.4M_\odot/M_0)^2$. Arrows represent the velocity field in the orbital plane. The black hole AH interior is marked by a filled black circle. The ADM mass for this case is $M = 2.5 \times 10^{-5}(M_0/1.4M_\odot)$ s= $7.6(M_0/1.4M_\odot)$km.
Bottom two plots: Snapshots of the entropy parameter K contours for cases A0 (left) and A4 (right). The light grey regions correspond to $1.4 < \log_{10} K < 2.6$, and the dark grey region corresponds to $2.6 < \log_{10} K < 3.8$.

wave kick at merger. There is a great deal of winding of magnetic fields threading the disk at this time (green lines), but no strong evidence of collimation around the BH poles or magnetic field turbulence in the disk. The lack of magnetic field turbulence may be due to insufficient resolution in the disk, which artificially suppresses instabilities like MRI. Insufficient resolution, coupled with the termination of the simulation after only $30(M_0/1.4M_\odot)$ms may explain why no magnetic field collimation was observed. The bottom left and center

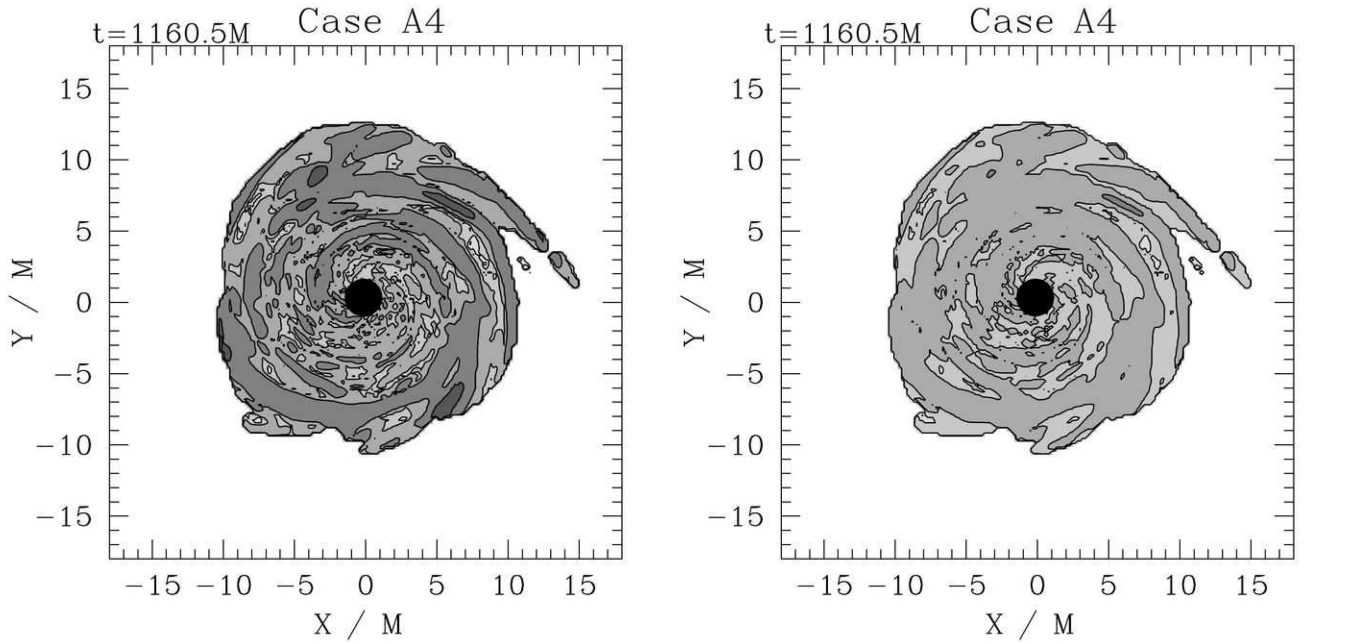

FIG. 10. $b^2/(2P)$ (left) and b^2 (right) contours, at the same time as Fig. 9, plotted according to $b^2/(2P) = 10^{-1.5}(10^{-1.3j})$, ($j$=0, 1, ... 5), and $\kappa b^2 = 10^{-5}(10^{-2.2j})$, ($j$=0, 1, ... 5). $b^2/(2P)$ and b^2 contours are only plotted for regions with densities higher than the lowest-density ρ_0 contours in Fig. 9. In cgs units, $\kappa^{-1} = 6 \times 10^{36} \mathrm{erg\,cm^{-3}} (1.4 M_\odot/M_0)^2$.

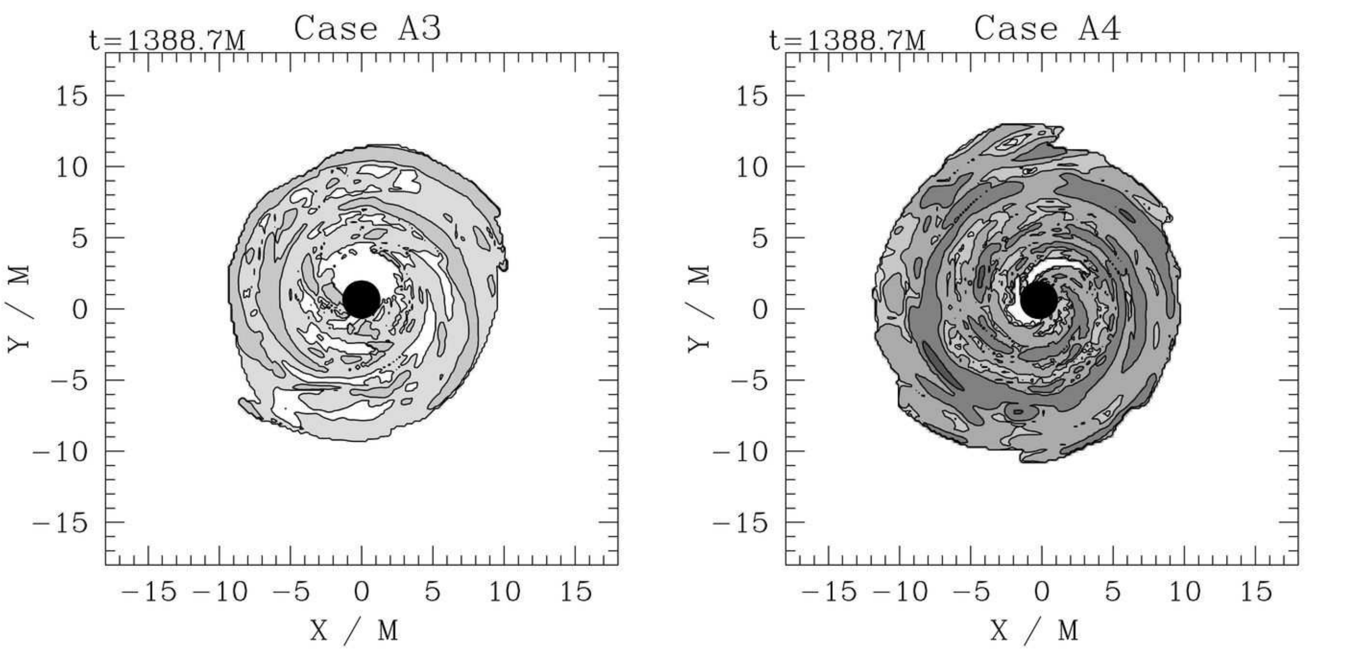

FIG. 11. $b^2/(2P)$ contours for cases A3 (left) and A4 (right), plotted according to $b^2/(2P) = 10^{-1.5}(10^{-1.3j})$, ($j$=0, 1, ... 5). Contours are only plotted for regions with densities above the low-density cutoff in Fig. 9.

frames of the figure show that a cavity has not formed around the BH by the end of the simulation. This result appears to be consistent with studies which suggest that stresses in magnetized disks may suppress the presence of an ISCO [95, 96]. However, longer, more accurate disk evolutions will be necessary to fully assess the agreement between these studies and simulations in full GR.

The strong seed magnetic fields in case B4 amplify the disk mass significantly, similar to case A4. Figure 16 demonstrates how the NS density contours are affected

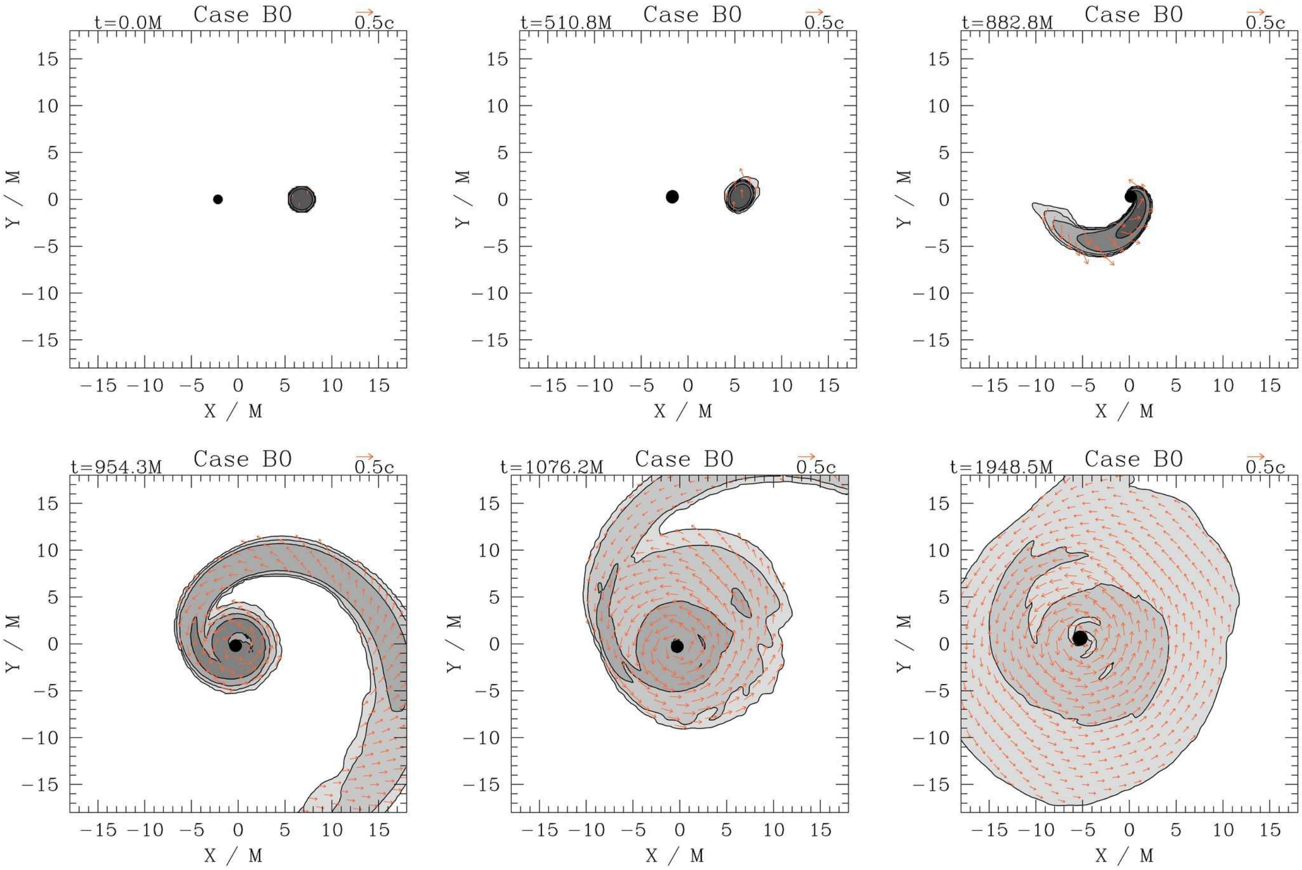

FIG. 12. Orbital-plane density contours at selected times for case B0. Density contours are plotted in the orbital plane, according to $\rho_0 = \rho_{0,\max}(10^{-0.92j})$, ($j$=0, 1, ... 5), with darker greyscaling for higher density. The maximum initial NS density is $\kappa\rho_{0,\max} = 0.126$, or $\rho_{0,\max} = 9 \times 10^{14}$g cm$^{-3}(1.4M_\odot/M_0)^2$. Arrows in density contour plots represent the velocity field in the orbital plane, and the black hole AH interior is marked by a filled black circle. The ADM mass for this case is $M = 2.5 \times 10^{-5}(M_0/1.4M_\odot)s= 7.6(M_0/1.4M_\odot)$km.

by such strong magnetic fields, comparing case B4 (right plot) with the unmagnetized case (left plot) shortly after tidal disruption. Although the seed magnetic fields are the same strength and geometry as in case A4 (cf. Fig. 6), the NS outer layers in case B4 are pushed out much more than in case A4. The magnetic pressure in case B4 does not rise above about 3% of the gas pressure in the orbital plane, as shown in Fig. 17 (left plot). This is consistent with case A4. Although $b^2/(2P)$ varies strongly throughout the NS, b^2 tends to be stronger in the densest regions of the NS (right plot), again similar to case A4 (cf. Fig. 10).

Figure 18 contrasts the distribution of rest-mass density and entropy ($\log K$) in the remnant disks of cases B0 and B4, at the time in which the B4 simulation was stopped. In the nonspinning cases A0 and A4 (Fig. 9), the sizes of the remnant disks in the orbital plane are remarkably similar, though the disk mass in case A4 is about twice A0's disk mass. The extra disk mass in case A4 may be explained by the existence of a high-density ring of matter in the disk. Unlike the nonspinning cases however, the high-density regions of the remnant disks in cases B0 and B4 are remarkably similar (upper plots). Despite this, B4's final disk possesses about 40% more mass than B0. Apparently the excess mass in case B4's disk comes from its larger volume. The size difference between B0 and B4's final disks is seen more clearly in the entropy contour plots (bottom two plots), which demonstrate the disks are hotter close to the BH and in the lowest-density outer regions.

Magnetic field amplitude contour plots for case B4's disk at the same time as Fig. 18 are displayed in Fig. 19. As in case A4, the final disk mass is greatly increased by strong magnetic fields, even though magnetic pressure never exceeds about 3% of the gas pressure, with typical values around 0.1% (left plot of Fig. 19). Bubbles of enhanced b^2, corresponding to order-of-magnitude increases in $|b|$, appear in a small ring around the BH and in the disk's outer regions (right plot of Fig. 19).

Finally, Fig. 20 compares B0 and B4 profiles in the meridional plane. As in the nonspinning cases, the geometry of the disk appears to be mostly unchanged by the addition of magnetic fields. There is small amount of material flowing into the BH from the poles, and the

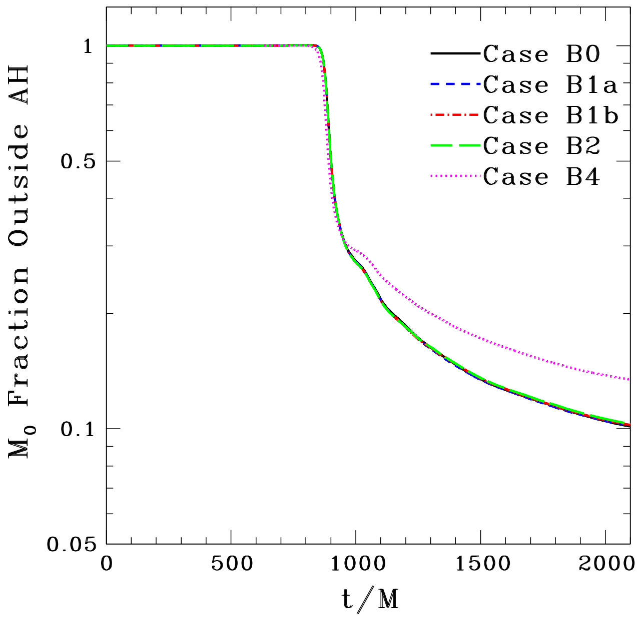

FIG. 13. Rest-mass fraction outside the AH for all cases in which the initial BH possesses spin parameter of $a_{\rm BH}/M_{\rm BH}$=0.75.

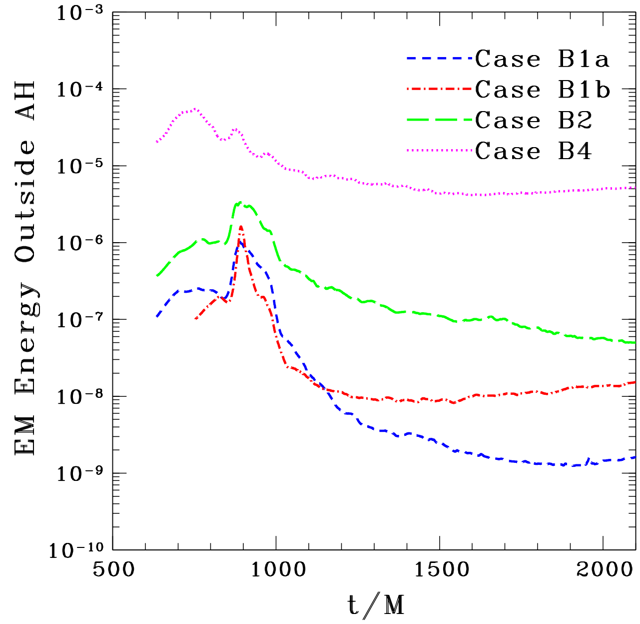

FIG. 14. Total magnetic energy outside the AH for all magnetized cases in which the initial BH possesses spin parameter of $a_{\rm BH}/M_{\rm BH}$=0.75, normalized by the ADM mass $M = 9.3 \times 10^{54}(M_0/1.4M_\odot)$erg..

magnetic fields are mainly confined inside the disk.

C. Gravitational Waves Study

Gravitational waves are extracted at several radii between $50M$ and $130M$. These radii are sufficiently far from the binary for the waves to overlap very well when plotted against retarded time, after accounting for the amplitude fall-off with radius. The upper panel of Fig. 21 shows the dominant (2,2) mode of the gravitational waveform as a function of retarded time $t_{\rm ret}$ for case A0, and the difference between the two data sets is displayed in the lower panel. The difference in amplitude between A0 and A4 waveforms is less than 3%, indicating that magnetic fields explored here do not significantly impact the global dynamics during BHNS inspiral and merger. By contrast, the difference between the B0 and B4 waveforms during merger is substantial (Fig. 22). The more highly spinning BHs of cases B0 and B4 possess smaller ISCOs, enabling NS to orbit the BH more closely before accreting, resulting in more gravitational wave cycles. Further, at smaller separations from the BH, the effects of frame dragging are much more pronounced, twisting NS matter around the BH and reducing the BH accretion rate, ultimately giving the magnetic fields more time to amplify and affect the global dynamics of NS matter.

However, the *observability* of magnetic effects on gravitational waveforms depends on the response of the GW detectors to the time series data. One way to assess the detectability is to compute the mismatch

$$MM \equiv 1 - \frac{(h_{B0}|h_{B4})}{\sqrt{(h_{B0}|h_{B0})(h_{B4}|h_{B4})}} \ , \qquad (28)$$

between the waveforms of B0 and B4, assuming the NS mass is 1.4 $M_\odot$, where

$$(h_1|h_2) = 4\,\mathrm{Re}\int_0^\infty \frac{\tilde{h}_1(f)\tilde{h}_2^*(f)}{S_h(f)}df. \qquad (29)$$

Here $h = h_+ - ih_\times$, $\tilde{h}$ is the Fourier transform of $h(t)$, and $S_h(f)$ is the power spectral density of the Advanced LIGO noise. Using the Advanced LIGO broadband configuration HIGH_DET_HIGH_P, the minimum mismatch (by varying the time and phase shifts between the two waveforms) between B0 and B4 waveforms is only 0.004, indicating that it may be challenging for Advanced LIGO broadband to detect the strong internal magnetic fields of case B4.

Complete GW spectra in the frequency domain require the creation of hybrid waveforms, which stitch together numerical and post-Newtonian (PN) waveforms. We generate hybrids by first computing the minimum of

$$\int_{t_{\rm i}}^{t_{\rm f}} dt \sqrt{\sum_{i\in\{+,\times\}} (h_i^{\rm NR} - h_i^{\rm PN})^2} \qquad (30)$$

via the Nelder-Mead algorithm, using as free parameters initial PN phase, amplitude, and orbital angular

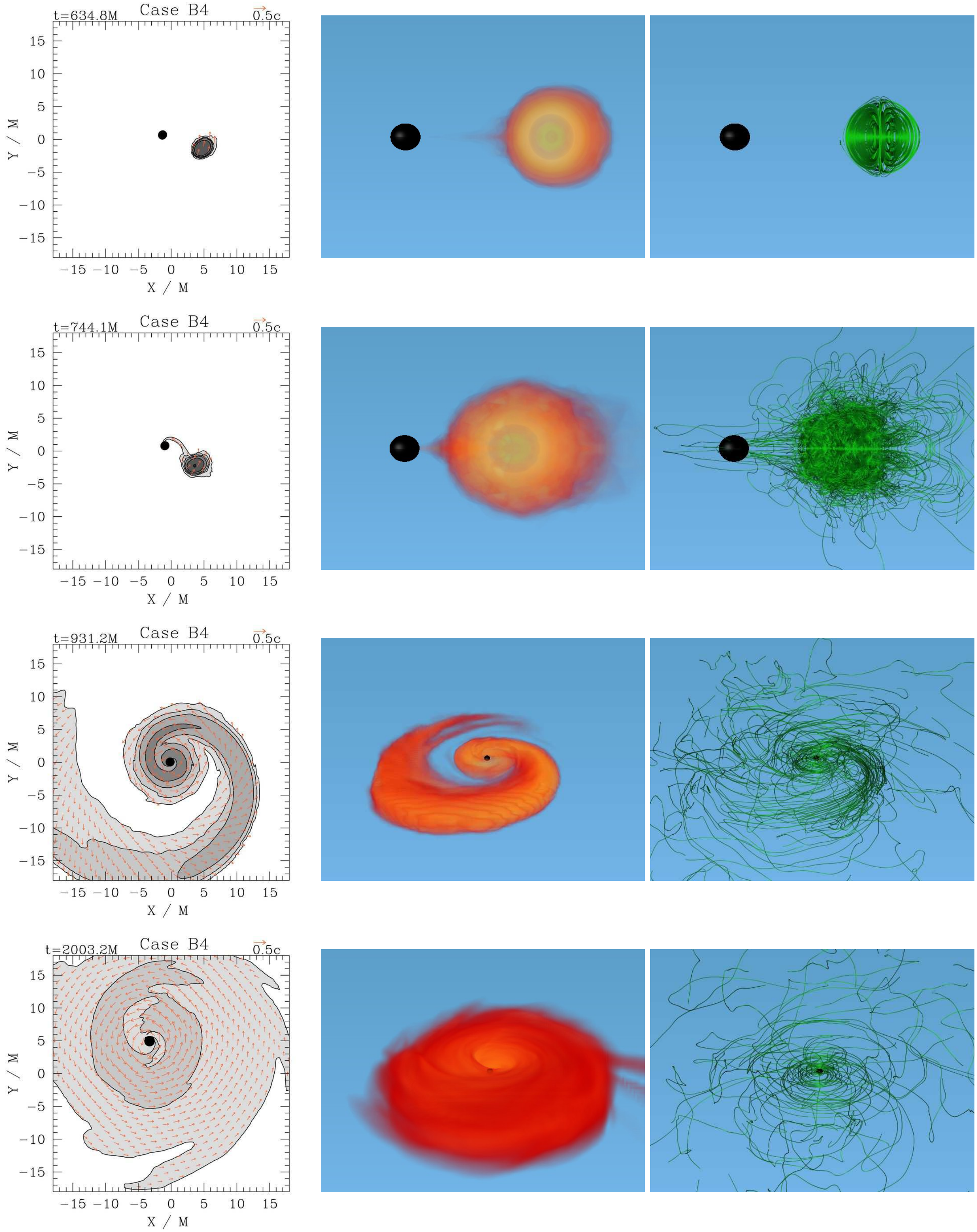

FIG. 15. Orbital-plane density contours (left column), 3D density profiles (middle column) and 3D magnetic field lines (right column) at four selected times for case B4. The times in the rows (top to bottom) are t/M =634.8, 744.1, 931.2, and 2003. Density contours in the orbital plane (left column) are plotted according to $\rho_0 = \rho_{0,\rm max}(10^{-0.92j})$, ($j$=0, 1, ... 5), with darker greyscaling for higher density. The maximum initial NS density is $\kappa\rho_{0,\rm max} = 0.126$, or $\rho_{0,\rm max} = 9 \times 10^{14}{\rm g\ cm}^{-3}(1.4M_\odot/M_0)^2$. Arrows in density contour plots represent the velocity field in the orbital plane, and the black hole AH interior is marked by a filled black circle. Magnetic fields are plotted as streamlines of the magnetic field vector B^i, distributed in proportion to $|B^i|$. The ADM mass for this case is $M = 2.5 \times 10^{-5}(M_0/1.4M_\odot)$s= $7.6(M_0/1.4M_\odot)$km.

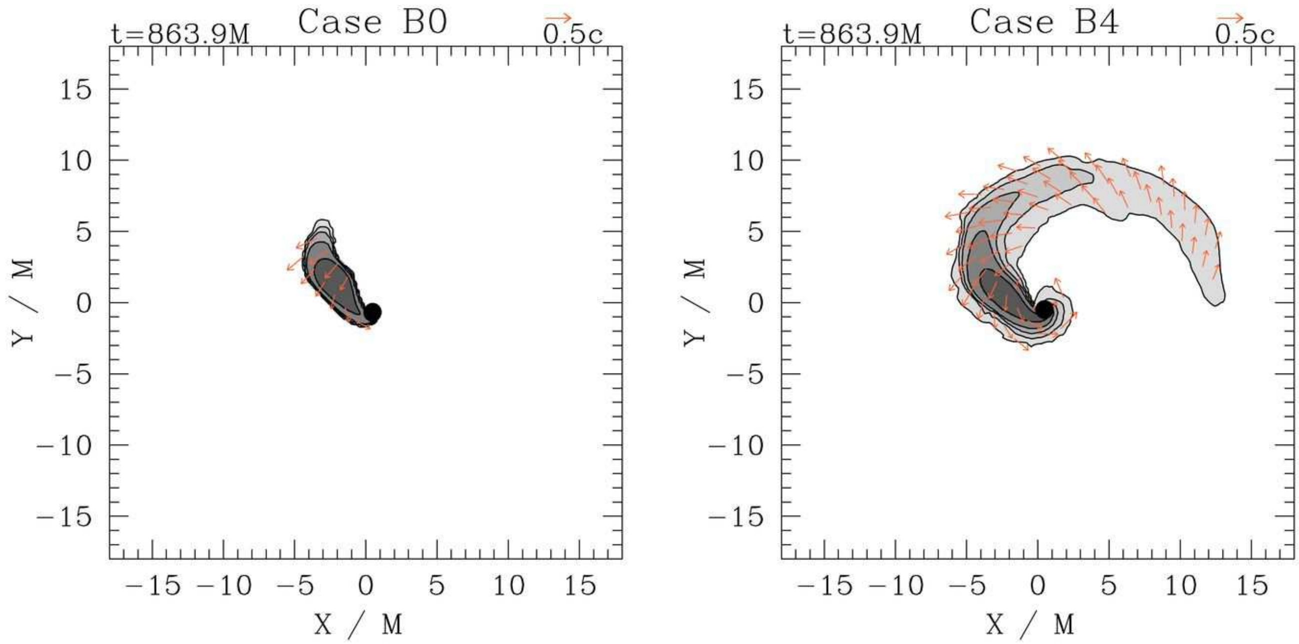

FIG. 16. Density and velocity profile snapshots during NS tidal disruption for cases B0 (left) and B4 (right). Density contours are plotted in the orbital plane according to $\rho_0 = \rho_{0,\max}(10^{-0.92j})$, ($j$=0, 1, ... 5), with darker greyscaling for higher density. The maximum initial NS density is $\kappa\rho_{0,\max} = 0.126$, or $\rho_{0,\max} = 9 \times 10^{14}$g cm$^{-3}(1.4M_\odot/M_0)^2$. Arrows represent the velocity field in the orbital plane, and the black hole AH interior is marked by a filled black circle. The ADM mass for this case is $M = 2.5 \times 10^{-5}(M_0/1.4M_\odot)$ s= $7.6(M_0/1.4M_\odot)$km.

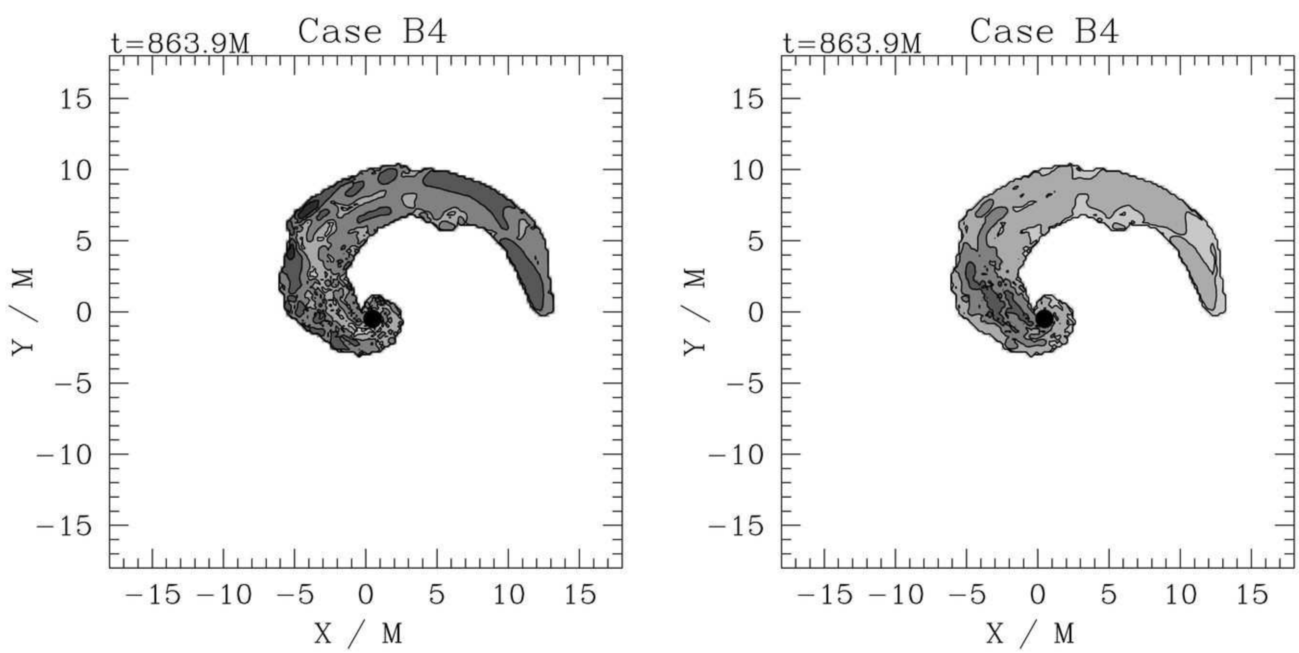

FIG. 17. Pressure ratio $b^2/(2P)$ (left) and magnetic pressure $b^2/2$ (right) contours during NS tidal disruption, at the same time as Fig. 16, plotted according to $b^2/(2P) = 10^{-1.5}(10^{-1.3j})$, ($j$=0, 1, ... 5), and $\kappa b^2 = 10^{-5}(10^{-2.2j})$, ($j$=0, 1, ... 5). Darker greyscaling denotes higher values. Contours are only plotted for regions with densities higher than the lowest-density ρ_0 contours in Fig. 16. In cgs units, $\kappa^{-1} = 6 \times 10^{36}$dyn cm$^{-2}(1.4M_\odot/M_0)^2$.

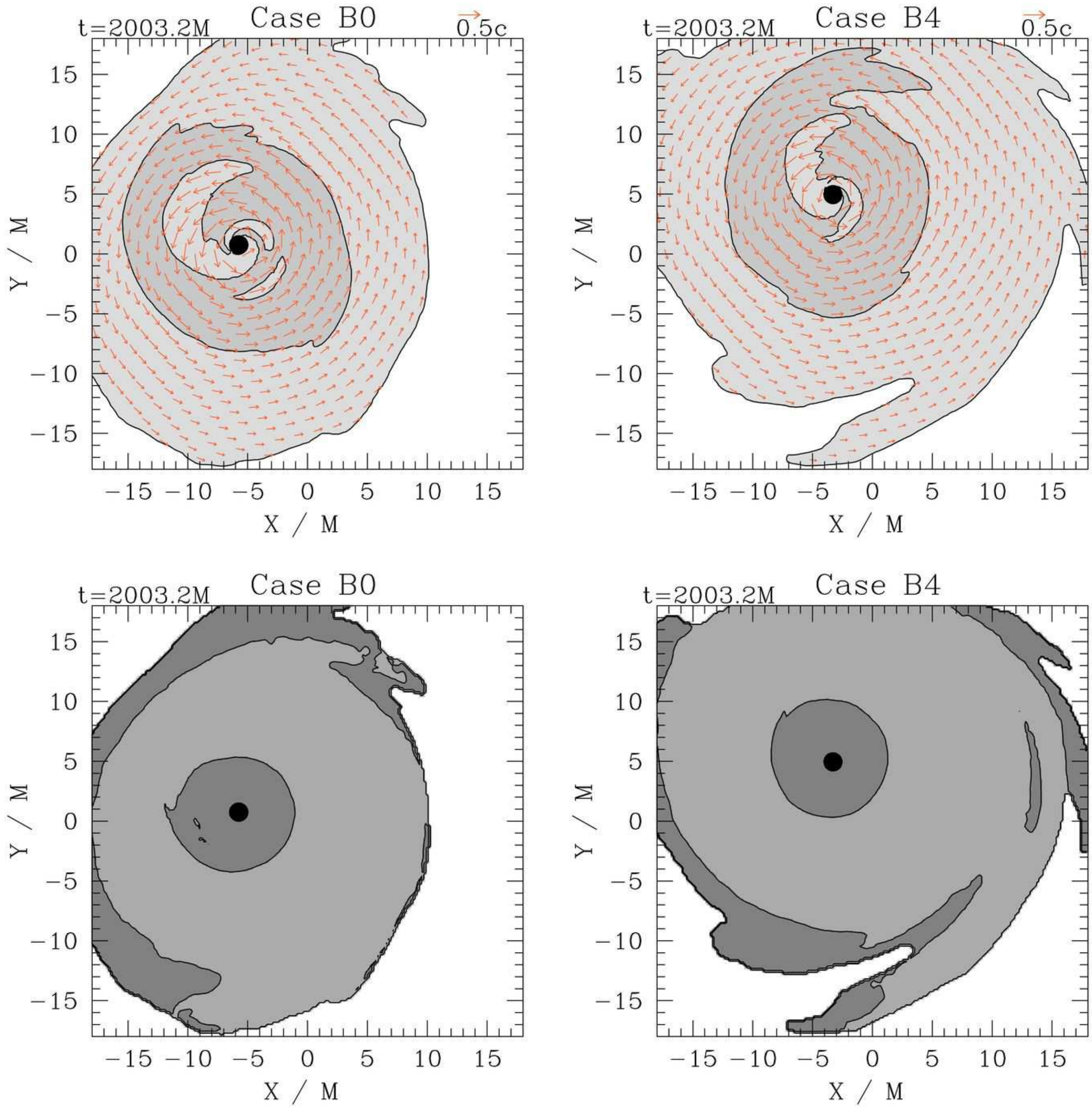

FIG. 18. Top two plots: Density and velocity profile snapshots at the time in which the B0 simulation is stopped, for cases B0 (left) and B4 (right). The contours represent the density in the orbital plane, plotted according to $\rho_0 = \rho_{0,\max}(10^{-0.92j})$, ($j$=0, 1, ... 5), with darker greyscaling for higher density. The maximum initial NS density is $\kappa\rho_{0,\max} = 0.126$, or $\rho_{0,\max} = 9 \times 10^{14}\mathrm{g\ cm}^{-3}(1.4M_\odot/M_0)^2$. Arrows represent the velocity field in the orbital plane. The black hole AH interior is marked by a filled black circle. The ADM mass for this case is $M = 2.5 \times 10^{-5}(M_0/1.4M_\odot)s= 7.6(M_0/1.4M_\odot)$km.
Bottom two plots: Snapshots of entropy parameter K contours for cases B0 (left) and B4 (right). The light grey regions correspond to $1.4 < \log_{10} K < 2.6$, and the dark grey region corresponds to $2.6 < \log_{10} K < 3.8$.

frequency. Here, $h^{\rm NR}_{+,\times}$ and $h^{\rm PN}_{+,\times}$ specify our numerical BHNS waveforms and the TaylorT1 PN waveforms of [99], respectively. The integration bounds were chosen to be $t_{\rm i} \approx 200M$ and $t_{\rm f} \approx 400M$. The hybrid waveform consists of a linear combination of the PN and NR waveforms, as in [100].

Effective GW strains of the hybrid waveforms in frequency space are plotted in Fig. 23 for A0, and Fig. 24 for cases B0 and B4. Assuming the NS has a rest mass of $1.4M_\odot$ and binary distance of 100Mpc, we plot

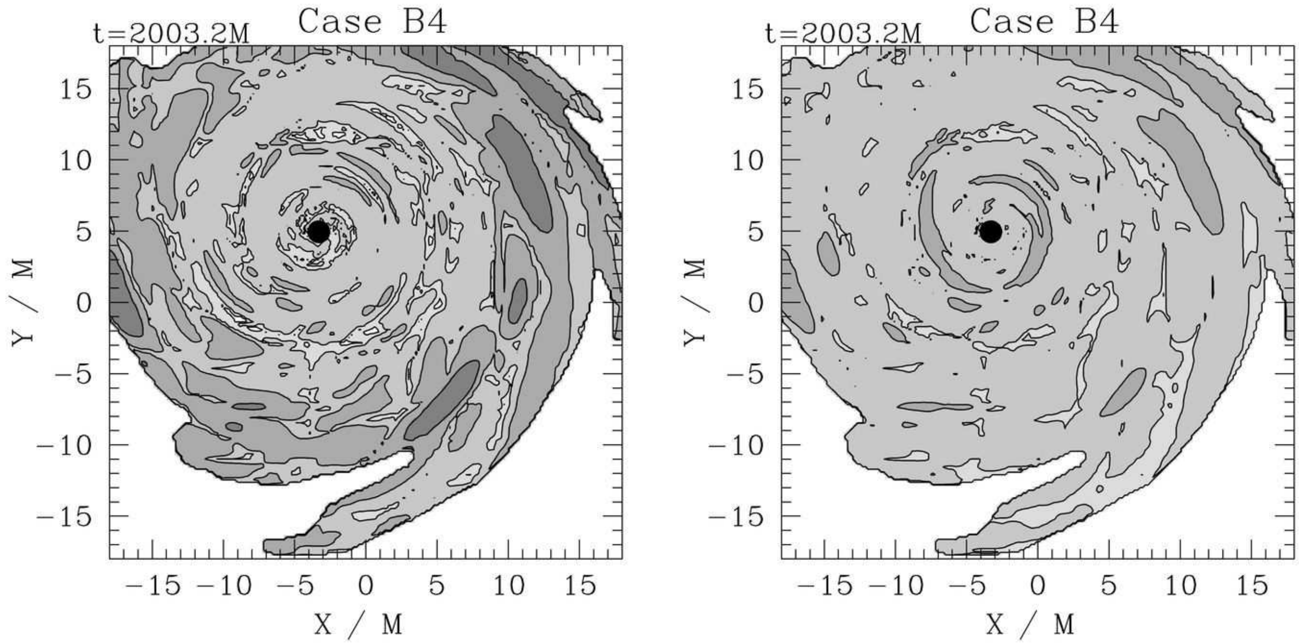

FIG. 19. Pressure ratio $b^2/(2P)$ (left) and magnetic pressure $b^2/2$ (right) contours, at the same time as Fig. 18, plotted according to $b^2/(2P) = 10^{-1.5}(10^{-1.3j})$, ($j$=0, 1, ... 5), and $\kappa b^2 = 10^{-5}(10^{-2.2j})$, ($j$=0, 1, ... 5). $b^2/(2P)$ and b^2 contours are only plotted for regions with densities higher than the lowest-density ρ_0 contours in Fig. 18. In cgs units, $\kappa^{-1} = 6 \times 10^{36}\mathrm{dyn\ cm}^{-2}(1.4M_\odot/M_0)^2$.

these strains against the Advanced LIGO sensitivity curve $h_{\rm LIGO}(f) \equiv \sqrt{fS_h(f)}$. Within this distance, the BHNS event rate is estimated to be 5×10^{-3}–10 per year, assuming an overall rate of 0.05–100 mergers per Myr per Milky Way-equivalent galaxy (and a density of 0.1 gal/Mpc^3) [29]. Cases A1–A4 and B1–B3 are not shown in the figures because their effective GW strains are almost indistiguishable from cases A0 and B0, respectively. Advanced LIGO in the chosen configuration may be able to marginally distinguish between BHNS waveforms and those produced by BHBH mergers at high frequencies (500–1000Hz). However, the effects of even the strongest magnetic fields chosen here (cases A4 and B4) on the waveforms are quite small and may be challenging for Advanced LIGO to detect in a broadband configuration. This is consistent with the result from the minimum mismatch calculation between B0 and B4, as mentioned above. Nevertheless, recent innovations exploring ‘squeezed light’ effects may reduce quantum noise and increase the sensitivity in this very domain [101].

It has been suggested that the differences between BHNS and BHBH waveforms during late inspiral and merger may be used to extract the tidal deformability of the NS [102], which can in turn be used to constrain the NS EOS. Our results suggest that seeding the NS with magnetic fields of the configurations and strengths explored here do not alter gravitational waveforms significantly. Further studies at higher resolution may be required to confirm this finding.

D. Energy and angular momentum conservation

We compute the energy $\Delta E_{\rm GW}$ and angular momentum $\Delta J_{\rm GW}$ carried away by the GWs, as well as the GW recoil velocity $v_{\rm kick}$. Violation of energy δE and angular momentum δJ, as defined in Eqs. (26) and (27), respectively, is also monitored. Results are given in Table III. For cases A0–A4, $\delta E \approx 0.2\%$ and $\delta J \approx 2\%$. Whereas for cases B0–B4, $\delta E \approx 0.6\%$ and $\delta J \approx 8\%$. In all cases, a fraction of E and J are lost spuriously, and the situation is slightly worse in spinning BH cases.

To further study the issue of E and J loss, we calculate the angular momentum inside the computational domain, $J_{\rm int}$, using Eq. (22), as well as the accumulated angular momentum carried away by the GWs, ΔJ_{GW}. Figures 25 and 26 show the evolution of $J_{\rm int}$ and ΔJ_{GW} for representative cases (A4 and B4). The corresponding plots for the various components of energy are similar. Conservation of angular momentum implies that $J_{\rm sum} = J_{\rm int} + \Delta J_{GW}$ is constant in time and is equivalent to the ADM angular momentum of the binary. Notice that the total angular momentum $J_{\rm sum}$ is conserved well during inspiral for both cases ($t_{\rm ret} \leq 500M$ for case A4 and $t_{\rm ret} \leq 700M$ for B4). Post-merger, ΔJ_{GW} flattens as GW emission subsides in all cases. $J_{\rm int}$ also flattens after merger in case A4, as expected. Hence the spurious loss of J ($\approx 2\%$) occurs primarily during merger for case A4. The same behavior is observed in cases A0–A3 as well. However, in cases B0–B4, $J_{\rm int}$ decreases on a secular timescale after

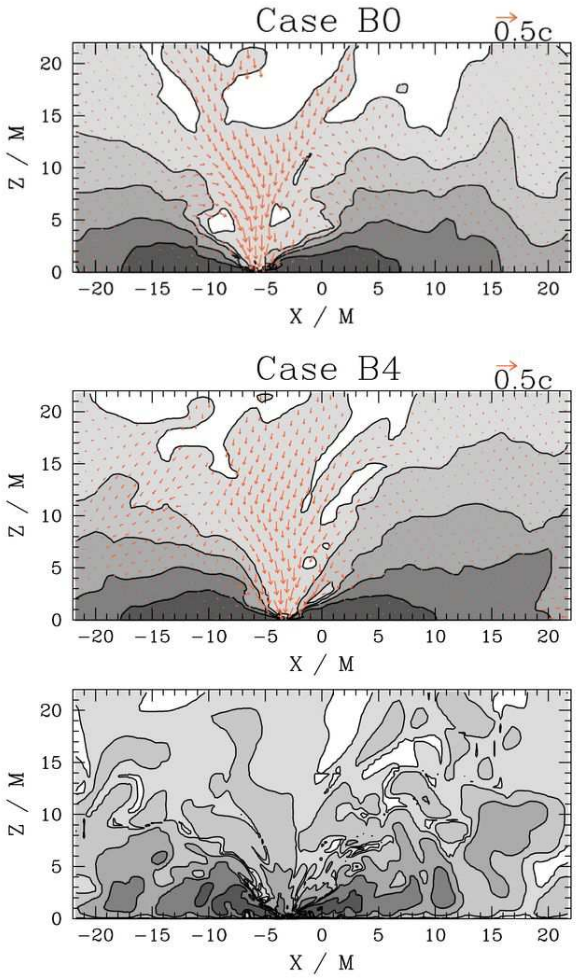

FIG. 20. Rest-mass density profile for case B0 (top), B4 (middle) and magnetic energy density b^2 (bottom) profiles for B4 in the meridional plane at the end of simulation ($t = 2003.2M$). Density contours are plotted according to $\rho_0 = \rho_{0,\max}10^{-7.6+0.717j}$, $(j = 0, ..., 6)$, with darker greyscaling for higher density. b^2 contours are plotted according to $\kappa b^2 = 10^{-12+0.833j}$, $(j = 0, ..., 6)$. The maximum initial NS density is $\kappa\rho_{0,\max} = 0.126$, or $\rho_{0,\max} = 9 \times 10^{14}\mathrm{g\ cm}^{-3}(1.4M_\odot/M_0)^2$. Arrows represent the velocity field in the meridional plane. In cgs units, the ADM mass for this case is $M = 2.5 \times 10^{-5}(M_0/1.4M_\odot)$ s= $7.6(M_0/1.4M_\odot)$km, and $\kappa^{-1} = 6 \times 10^{36}\mathrm{erg\ cm}^{-3}(1.4M_\odot/M_0)^2 = 7 \times 10^{15}\mathrm{g\ cm}^{-3}(1.4M_\odot/M_0)^2$.

merger. The value of $J_{\rm sum}$ deviates from its initial value by about 2% after the merger at $t_{\rm ret} \approx 900M$, but the deviation increases slowly and reaches $\approx 7\%$ at the end of simulation ($t_{\rm ret} = 2000M$), indicating that the spurious loss of J continues after merger in case B4.

The BH spin parameter for case B4 increases from $a_{\rm BH}/M_{\rm BH}$ =0.75 to $\approx$ 0.85 during the simulation (see Table III). A secular decrease of total angular momentum as found in case B4 is commonly observed in rapidly spinning vacuum BH simulations (see e.g., [103]), which find that spurious J loss is reduced with increasing resolution.

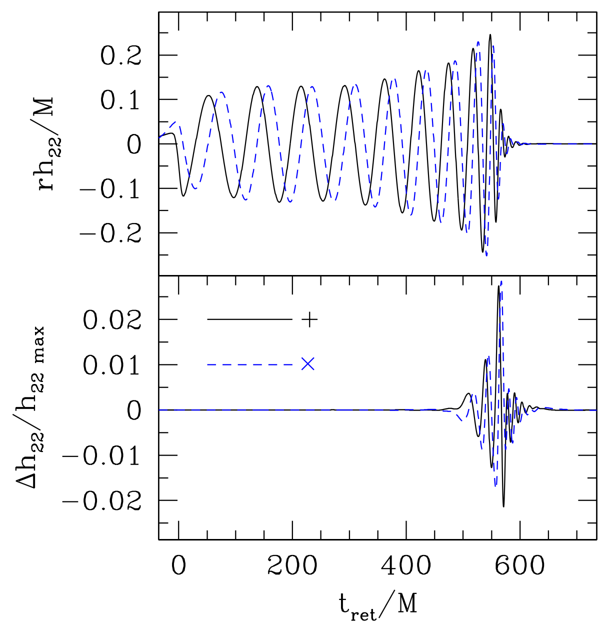

FIG. 21. Upper panel: (2,2) mode of the gravitational wave strain h^+_{22} (solid line) and $h^\times_{22}$ (dashed line) versus retarded time $t_{\rm ret}$ for case A0.
Lower panel: difference in h^+_{22} (solid line) and $h^\times_{22}$ (dashed line) between cases A0 and A4 versus $t_{\rm ret}$, normalized by the maximum value of $|h^+_{22} - ih^\times_{22}|$ for case A0 over time, $h_{22\,\max}$.

Figures 25 and 26 also show the evolution of the BH's angular momentum $J_{\rm BH}$, computed using the isolated and dynamical horizon formalism. $J_{\rm BH}$ monotonically increases in both A4 and B4, and is always less than $J_{\rm int}$. This seems to suggest that the spurious loss of J in case B4 after merger may occur mainly in the remnant disk, where a substantial amount of matter is continuously crossing the refinement levels. However, the possibility of spurious loss of J in the strong-field region near the BH cannot be ruled out completely. One way to resolve the issue would be to compute the amount of J flowing into the BH and check for the conservation of J at the BH horizon (see e.g., Sec. 4.2 of [90]).

V. SUMMARY AND FUTURE WORK

We present preliminary results from magnetized simulations of BHNS binaries with BH:NS mass ratio 3:1. We treat both initially nonspinning (cases A) and moderately-spinning (cases B) BHs. For those magnetic field configurations we consider, only initial NS magnetic fields with maximum (internal) strength of $\approx 10^{17}$G – corresponding to average magnetic to gas pressure ratio of 0.5% – significantly impact the inspiral and merger dynamics. During merger, most of the magnetized NS matter is captured by the BH. After disruption, the dynam-

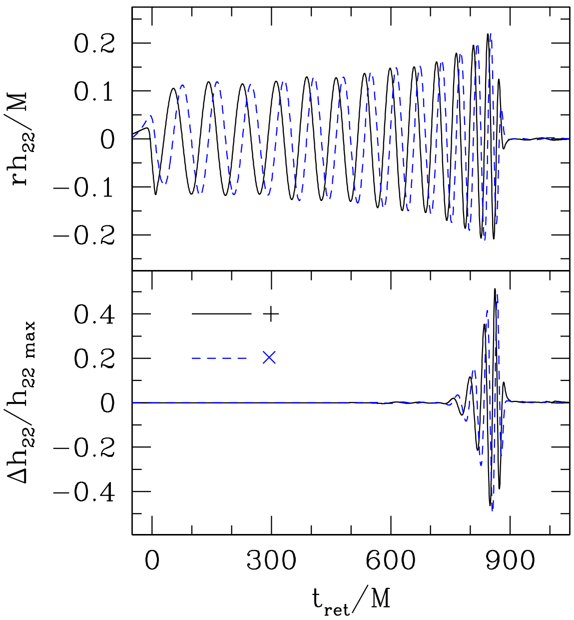

FIG. 22. Same as Fig. 21 but for cases B0 and B4.

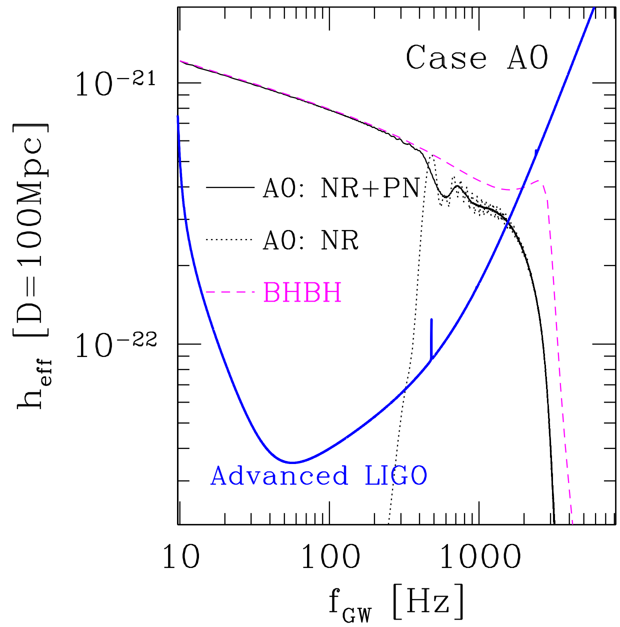

FIG. 23. Gravitational-wave power spectrum for case A0 computed as in Sec. IIIF of [25]. The solid curve shows the power spectrum of the numerical signal (dotted curve) stitched to the post-Newtonian waveform, including only the dominant $(2,2)$ and $(2,-2)$ modes. The dashed curve shows the power spectrum expected from BHBH binaries with the same total mass and mass ratio as the BHNS, derived in [97] from analysis of multi-orbit, non-precessing BHBH binaries. The heavy solid curve displays the effective strain of the Advanced LIGO detector, defined such that $h_{\rm LIGO}(f) \equiv \sqrt{f S_h(f)}$. The noise curve used here corresponds to the Advanced LIGO configuration ZERO_DET_HIGH_P [98]. To set physical units, a NS rest mass of $M_0 = 1.4 M_\odot$ and a source distance of D=100Mpc is assumed.

ics are followed for about 30–50 $(M_0/1.4M_\odot)$ms. Only in the cases in which magnetic fields are strongest are magnetic effects dynamically significant, increasing the final disk mass by up to a factor of two. The strong magnetic fields help push out the outer layers of the NS during tidal disruption, resulting in a gravitational wave mismatch of 0.004 for the Advanced LIGO broadband configuration. It may be challenging for the upcoming generation of gravitational wave detectors to observe effects from such magnetic fields. Further studies with different field geometries, black hole spins and higher resolution may be required to confirm this finding.

Some SGRB models require a massive, hot, magnetized disk around a BH with collimated magnetic fields to launch jets that generate γ-rays (see, e.g. [53, 54]). In our BHNS simulations, the remnant disk is hot ($T \sim 1$MeV) and massive ($M_{\rm disk} \sim 0.02 M_\odot$ and $\sim 0.1 M_\odot$ for cases A and B, respectively), and possesses magnetic fields that are tightly wound. However, evidence for magnetic collimation around the BH or magnetic field-induced turbulence in the disk is not observed. Future analyses will focus on mode growth studies and B-field decomposition in poloidal and toroidal components with respect to the centre of mass of the NS, similar to previous studies of single rotating or magnetized stars [104–106]. The lack of collimation may be due to the short disk evolution time before our simulation is terminated. The absence of turbulence in the disk may be due to insufficient resolution in the disk, thereby suppressing instabilities like MRI. Therefore, future work will focus on evolving the disk at higher resolution, coupled with longer disk evolutions and different initial magnetic field configurations to more thoroughly assess the possibility of BHNS binaries as short-hard GRB progenitors.

ACKNOWLEDGMENTS

The authors wish to thank Charles F. Gammie for useful discussions. We also thank the Illinois Relativity Group's Research Experience for Undergraduates (REU) team, including Gregory Colten, Stephen Drake, Miaotianzi Jin, David Kolschowsky, David Kotan, and Francis Walsh, for assistance in producing the 3D visualizations of our simulations. This paper was supported in part by NSF Grants AST-1002667, and PHY-0963136 as well as NASA Grant NNX10AI73G at the University of Illinois at Urbana-Champaign.

Appendix A: Hydrodynamic and MHD inequalities

For a given set of "primitive" variables (ρ_0, P, v^i, B^i) in the physical range (i.e. $\rho_0 \geq 0$, $P \geq 0$ and $\epsilon \geq 0$),

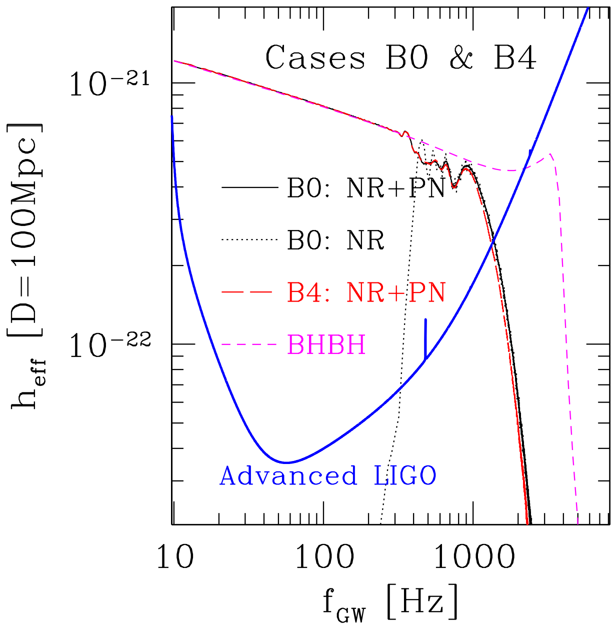

FIG. 24. Same as Fig. 23 but for Cases B0 and B4.

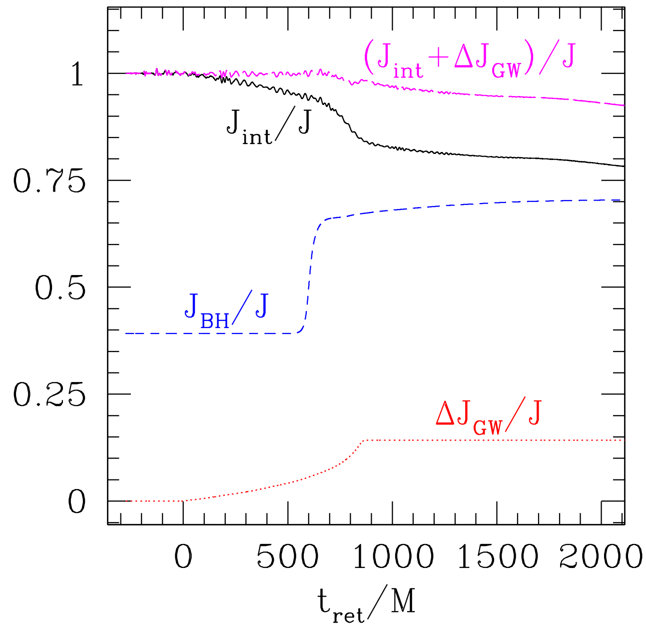

FIG. 26. Same as Fig. 25 but for case B4.

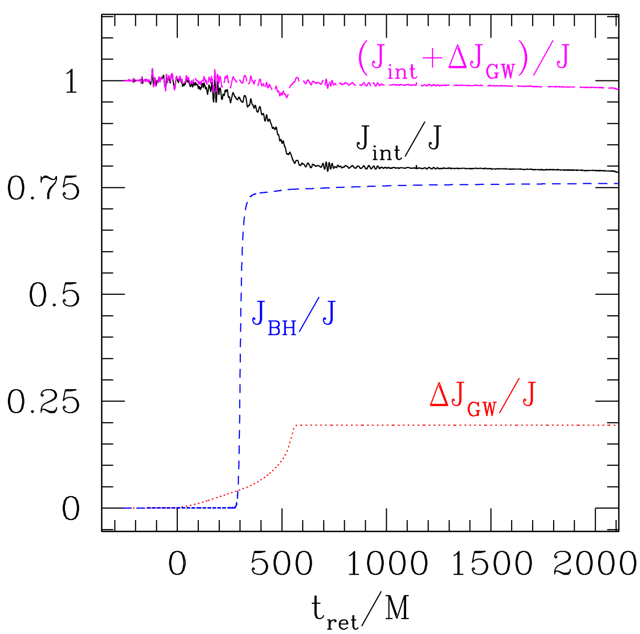

FIG. 25. Evolution of interior angular momentum $J_{\rm int}$, angular momentum carried off by GW $\Delta J_{\rm GW}$, and BH's angular momentum $J_{\rm BH}$ for case A4. All quantities are normalized by the ADM angular momentum of the binary J.

the corresponding "conservative" variables $(\rho_*, \tilde{\tau}, \tilde{S}_i, \tilde{B}^i)$ must satisfy certain inequalities. In this appendix, we derive the inequalities and provide a practical recipe to impose these inequalities approximately to reduce inversion failures, which occur mainly in regions with very low density in the artificial "atmosphere" or inside the BH horizon where high accuracy is difficult to maintain but not crucial. Even when applying this recipe, inversion failures sometimes occur. In that case, we employ an alternative inversion scheme, described in Sec. A 4, that always works. Readers who are only interested in our recipe may jump directly to Sec. A 3 and skip the rest of this appendix outlining the derivation.

Since the inversion between $\tilde{B}^i$ and B^i is trivial and does not involve other primitive variables, we will treat values of B^i as given and only consider the inversion from $(\rho_*, \tilde{\tau}, \tilde{S}_i)$ to (ρ_0, P, v^i). We assume that the EOS $P = P(\rho_0, \epsilon)$ always gives $P \geq 0$ whenever $\rho_0 \geq 0$ and $\epsilon \geq 0$. We also assume that the metric, lapse and shift are in the physical range. In particular, we require $\alpha > 0$ and $\gamma_{ij} k^i k^j > 0$ for any real vector k^i. The requirement $\alpha > 0$ is always satisfied by our particular time slicing. However, γ_{ij} may lose positive-definiteness due to numberical error during the evolution, especially in the region deep inside the BH, near the "puncture". Before performing the inversion, we check if γ_{ij} is positive definite by finding its eigenvalues. If γ_{ij} is not positive definite, we reset $\gamma_{ij} \to \psi^4 f_{ij}$ during the inversion, where f_{ij} is the 3D flat metric tensor.

1. Derivation of conservative variable inequalities: Pure hydrodynamic case

In the absence of magnetic fields, the conservative variables are given by

$$\rho_* = \sqrt{\gamma}\rho_0\gamma_v \tag{A1}$$
$$\tilde{S}_i = \rho_* h u_i \tag{A2}$$
$$\tilde{\tau} = h(w-\rho_*) + (h-1)\rho_* - \sqrt{\gamma}\, P, \tag{A3}$$

where

$$\gamma_v = \alpha u^0 \quad , \quad w = \gamma_v \rho_*, \tag{A4}$$

and $h = 1 + \epsilon + P/\rho_0 \geq 1$. It follows from $u_\mu u^\mu = -1$ that

$$\gamma_v = \sqrt{1+\gamma^{ij}u_i u_j}. \tag{A5}$$

Since $\gamma^{ij}u_i u_j$ is positive definitive, $\gamma_v \geq 1$. We therefore conclude that

$$\rho_* \geq 0 \tag{A6}$$

for $\rho_0 \geq 0$ and $u_i \in (-\infty, \infty)$. In addition, $w = \gamma_v \rho_* \geq \rho_*$, from which we obtain

$$\begin{aligned}\tilde{\tau} &\geq (h-1)\rho_* - \sqrt{\gamma}\, P \\ &= \sqrt{\gamma}[\gamma_v \rho_0 \epsilon + (\gamma_v - 1)P] \geq 0.\end{aligned} \tag{A7}$$

Hence we conclude that

$$\tilde{\tau} \geq 0, \tag{A8}$$

which is Eq. (15).

To derive the inequality (18), Eqs. (A2) and (A5) are combined to yield

$$\tilde{S}^2 = \gamma^{ij}\tilde{S}_i\tilde{S}_j = (\rho_* h)^2(\gamma_v^2 - 1) = h^2(w^2 - \rho_*^2). \tag{A9}$$

A straightforward calculation yields

$$\begin{aligned}(\tilde{\tau}+\rho_*)^2 &= \tilde{S}^2 + h^2\rho_*^2 - \sqrt{\gamma}\, P(2hw - \sqrt{\gamma}\, P) \\ &= \tilde{S}^2 + (\gamma_v\sqrt{\gamma})^2[\rho_0^2(1+\epsilon)^2 - P^2] \\ &\quad +(\sqrt{\gamma}\, P)^2\ .\end{aligned} \tag{A10}$$

Since there is no upper limit on γ_v, the sum of the second and third terms is always positive if and only if the dominant energy condition – $P^2 \leq \rho_0^2(1+\epsilon)^2$ – holds. Hence we conclude that

$$\tilde{S}^2 \leq (\tilde{\tau}+\rho_*)^2, \tag{A11}$$

if the dominant energy condition is satisfied. The inequality (18) is more stringent, and hence more useful. It can be derived using Eq. (A10):

$$\tilde{\tau}(\tilde{\tau}+2\rho_*) = \tilde{S}^2 + (\gamma_v\sqrt{\gamma})^2(2\rho_0^2\epsilon + \rho_0^2\epsilon^2 - P^2) + (\sqrt{\gamma}\, P)^2.$$

In this case, the sum of the second and third terms is always positive if and only if $P^2 \leq 2\rho_0^2\epsilon + \rho_0^2\epsilon^2$. Hence we have derived the inequality (Eq. 18):

$$\tilde{S}^2 \leq \tilde{\tau}(\tilde{\tau}+2\rho_*) \quad \text{iff } P^2 \leq 2\rho_0^2\epsilon + \rho_0^2\epsilon^2. \tag{A12}$$

Whether the condition $P^2 \leq 2\rho_0^2\epsilon + \rho_0^2\epsilon^2$ is satisfied depends on the EOS. For the Γ-law EOS $P = (\Gamma-1)\rho_0\epsilon$, simple calulation gives

$$P^2 - 2\rho_0^2\epsilon - \rho_0^2\epsilon^2 = \rho_0^2\epsilon[\Gamma(\Gamma-2)\epsilon - 2]. \tag{A13}$$

Hence the inequality $\tilde{S}^2 \leq \tilde{\tau}(\tilde{\tau}+2\rho_*)$ holds iff $\Gamma(\Gamma-2)\epsilon - 2 \leq 0$. Restricting to the parameter space where the sound speed is subluminal, i.e. $c_s^2 = \Gamma P/(\rho_0 h) < 1$, we have $\Gamma(\Gamma-2)\epsilon < 1$. Therefore, $\tilde{S}^2 \leq \tilde{\tau}(\tilde{\tau}+2\rho_*)$ holds for the Γ-law EOS in regions where the sound speed is subluminal. For the Γ-law EOS it can be shown that $c_s^2 < \Gamma - 1$ holds for any nonnegative ρ_0 and P. Thus, the sound speed will always be subluminal when $1 < \Gamma \leq 2$. Thus, $\tilde{S}^2 \leq \tilde{\tau}(\tilde{\tau}+2\rho_*)$ is satisfied for the Γ-law EOS, when $1 < \Gamma \leq 2$.

We have just proved that the inequalities $\rho_* \geq 0$, $\tilde{\tau} \geq 0$ and $\tilde{S}^2 \leq \tilde{\tau}(\tilde{\tau}+2\rho_*)$ are *necessary* conditions for the primitive inversion to yield a physical solution for $1 < \Gamma \leq 2$. We now want to prove that they are also the *sufficient* conditions for the Γ-law EOS with $\Gamma > 1$. For the Γ-law EOS, the enthalpy is related to the pressure P by

$$h = 1 + \frac{\Gamma P}{(\Gamma-1)\rho_0}. \tag{A14}$$

Combining the above equation with Eq. (A3) yields

$$h = \frac{\Gamma w(\tilde{\tau}+\rho_*) - (\Gamma-1)\rho_*^2}{\Gamma w^2 - (\Gamma-1)\rho_*^2}. \tag{A15}$$

It is useful to define a variable $x \equiv (w-\rho_*)/\tilde{\tau}$. It follows from Eqs. (A15) and (A9) that

$$h - 1 = \frac{\Gamma\tilde{\tau}(1-x)(x\tilde{\tau}+\rho_*)}{\Gamma\tilde{\tau}x(\tilde{\tau}x+2\rho_*)+\rho_*^2} \tag{A16}$$

and

$$f(x) \equiv \tilde{\tau}x(\tilde{\tau}x+2\rho_*) - \frac{\tilde{S}^2}{h^2} = 0. \tag{A17}$$

These two equations can be combined to yield a quartic equation in x. However, it is easier to analyze the equations in the present form. For any given $\rho_* \geq 0$, $\tilde{\tau} \geq 0$ and $\tilde{S}^2 \leq \tilde{\tau}(\tilde{\tau}+2\rho_*)$, when $x = 0$, $h = 1 + \Gamma\tilde{\tau}/\rho_* \geq 1$ and $f(0) = -\tilde{S}^2/h^2 \leq 0$; when $x = 1$, $h = 1$ and $f(1) = \tilde{\tau}(\tilde{\tau}+2\rho_*) - \tilde{S}^2 \geq 0$. Hence the intermediate value theorem implies there exists $x_0 \in [0,1]$ so that $f(x_0) = 0$. The primitive variables are recovered from the following expressions

$$\gamma_v = \frac{w}{\rho_*} = 1 + \frac{\tilde{\tau} x_0}{\rho_*}, \tag{A18}$$

$$\rho_0 = \frac{\rho_*}{\gamma_v \sqrt{\gamma}}, \tag{A19}$$

$$h - 1 = \frac{\Gamma\tilde{\tau}(1-x_0)(x_0\tilde{\tau}+\rho_*)}{\Gamma\tilde{\tau}x_0(\tilde{\tau}x_0+2\rho_*)+\rho_*^2}, \tag{A20}$$

$$P = \frac{\Gamma-1}{\Gamma}\rho_0(h-1), \tag{A21}$$

$$u_i = \frac{\tilde{S}_i}{\rho_* h}, \tag{A22}$$

$$v^i = \frac{\alpha}{\gamma_v}\gamma^{ij}u_j - \beta^i. \tag{A23}$$

Upon inspection, all the recovered primitive variables lie in the physically acceptable range for $x_0 \in [0,1]$ and $\Gamma > 1$.

We therefore conclude that the inequalities $\rho_* \geq 0$, $\tilde{\tau} \geq 0$ and $\tilde{S}^2 \leq \tilde{\tau}(\tilde{\tau}+2\rho_*)$ are both necessary and sufficient conditions for the inversion to yield physically-acceptable primitive variables for the Γ-law EOS with $1 < \Gamma \leq 2$. Since the Γ-law EOS with $\Gamma = 2$ is adopted in our simulations, we impose these inequalities in regions where there are no magnetic fields.

2. Derivation of conservative variable inequalities: MHD case

In the presence of magnetic fields, the conservative variables $\tilde{S}_i$ and $\tilde{\tau}$ are given by

$$\tilde{S}_i = \tilde{S}_i^{\rm fluid} + \alpha\sqrt{\gamma}\,(b^2u^0u_i - b^0b_i), \tag{A24}$$

$$\tilde{\tau} = \tilde{\tau}_{\rm fluid} + \sqrt{\gamma}\left[\gamma_v^2 b^2 - \frac{b^2}{2} - (\alpha b^0)^2\right]. \tag{A25}$$

Here $\tilde{S}_i^{\rm fluid} = \rho_* h u_i$ and $\tilde{\tau}_{\rm fluid} = h(w-\rho_*) + (h-1)\rho_* - \sqrt{\gamma}\,P$, which are the same expressions as Eqs. (A2) and (A3). The variable $\rho_* = \gamma_v\sqrt{\gamma}\,\rho_0$ remains unchanged and hence the inequality $\rho_* \geq 0$ still holds in the presence of magnetic fields.

It is convenient to introduce the following three quantities

$$W \equiv \gamma_v^2\rho_0 h = wh/\sqrt{\gamma} = \frac{\sqrt{\tilde{S}^2_{\rm fluid} + (\rho_* h)^2}}{\sqrt{\gamma}}, \tag{A26}$$

$$V \equiv \sqrt{\gamma_v^2 - 1}/\gamma_v, \tag{A27}$$

$$\bar{B}^i \equiv B^i/\sqrt{4\pi}. \tag{A28}$$

Following the algebra in Sec. 3.1 of [87], one can show that (c.f. Eqs. (26), (27) and (29) of [87])

$$\bar{B}^i\tilde{S}_i = \bar{B}^i\tilde{S}_i^{\rm fluid}, \tag{A29}$$

$$\tilde{S}^2 = (\sqrt{\gamma})^2V^2(W+\bar{B}^2)^2 - \frac{(\bar{B}^i\tilde{S}_i)^2(\bar{B}^2+2W)}{W^2}, \tag{A30}$$

$$\tilde{\tau} = \tilde{\tau}_{\rm fluid} + \frac{\sqrt{\gamma}}{2}(1+V^2)\bar{B}^2 - \frac{(\bar{B}^i\tilde{S}_i)^2}{2\sqrt{\gamma}\,W^2}, \tag{A31}$$

where $\bar{B}^2 = \gamma_{ij}\bar{B}^i\bar{B}^j$. It follows from Eq. (A29) and the Cauchy-Schwartz inequality that

$$\begin{aligned}(\bar{B}^i\tilde{S}_i)^2 &= (\gamma^{ij}\bar{B}_i\tilde{S}_j^{\rm fluid})^2 \\ &\leq (\gamma^{ij}\bar{B}_i\bar{B}_j)(\gamma^{ij}\tilde{S}_i^{\rm fluid}\tilde{S}_j^{\rm fluid}) \\ &= \bar{B}^2\tilde{S}^2_{\rm fluid}.\end{aligned}$$

Hence we obtain

$$\tilde{S}^2_{\rm fluid} \geq (\hat{\bar{B}}^i\tilde{S}_i)^2, \tag{A32}$$

where $\hat{\bar{B}}^i \equiv \bar{B}^i/\bar{B}$.

Using Eq. (A30), we can write

$$V^2 = \frac{1}{\gamma(W+\bar{B}^2)^2}\left[\tilde{S}^2 + \frac{(\bar{B}^i\tilde{S}_i)^2(\bar{B}^2+2W)}{W^2}\right], \tag{A33}$$

and

$$\tilde{S}^2_{\rm fluid} = \gamma V^2W^2 = \frac{W^2\tilde{S}^2 + (\bar{B}^i\tilde{S}_i)^2(\bar{B}^2+2W)}{(W+\bar{B}^2)^2}. \tag{A34}$$

Given values of $\tilde{S}_i$ and $\bar{B}^i$, the only independent variable in the above equation is W. Straightforward calculation yields

$$\frac{d\tilde{S}^2_{\rm fluid}}{dW} = \frac{2W[\bar{B}^2\tilde{S}^2 - (\bar{B}^i\tilde{S}_i)^2]}{(W+\bar{B}^2)^3} \geq 0, \tag{A35}$$

where we have applied the Cauchy-Schwarz inequality

$$(\bar{B}^i\tilde{S}_i)^2 = (\gamma^{ij}\bar{B}_i\tilde{S}_j)^2 \leq (\gamma^{ij}\bar{B}_i\bar{B}_j)(\gamma^{ij}\tilde{S}_i\tilde{S}_j) = \bar{B}^2\tilde{S}^2.$$

Hence the maximum value of $\tilde{S}^2_{\rm fluid}$ is achieved when $W \to \infty$, which gives $\tilde{S}^2_{\rm fluid} \leq \tilde{S}^2$. The minimum value of $\tilde{S}^2_{\rm fluid}$ is achieved when $W = W_m$, where W_m is the minimum value of W for given values of ρ_*, $\tilde{S}_i$ and $\bar{B}^i$. Hence we obtain

$$\tilde{S}^2_m \leq \tilde{S}^2_{\rm fluid} \leq \tilde{S}^2, \tag{A36}$$

where

$$\tilde{S}^2_m = \frac{W_m^2\tilde{S}^2 + (\bar{B}^i\tilde{S}_i)^2(\bar{B}^2+2W_m)}{(W_m+\bar{B}^2)^2}. \tag{A37}$$

The upper and lower bounds of $\tilde{\tau}_{\rm fluid}$ can be derived by first combining Eqs. (A31) and (A33):

$$\tilde{\tau}_{\rm fluid} = \tilde{\tau} - \frac{\sqrt{\gamma}}{2}\bar{B}^2 - \frac{\bar{B}^2\tilde{S}^2 - (\bar{B}^i\tilde{S}_i)^2}{2\sqrt{\gamma}\,(W+\bar{B}^2)^2}. \tag{A38}$$

For fixed values of $\tilde{\tau}$, $\tilde{S}_i$ and $\bar{B}^i$, $\tilde{\tau}_{\rm fluid}$ increases with increasing W. Therefore, we conclude that

$$\tilde{\tau}_m \leq \tilde{\tau}_{\rm fluid} \leq \tilde{\tau} - \frac{\sqrt{\gamma}}{2}\bar{B}^2, \tag{A39}$$

where

$$\tilde{\tau}_m = \tilde{\tau} - \frac{\sqrt{\gamma}}{2}\bar{B}^2 - \frac{\bar{B}^2\tilde{S}^2 - (\bar{B}^i\tilde{S}_i)^2}{2\sqrt{\gamma}\,(W_m+\bar{B}^2)^2}. \tag{A40}$$

To calculate W_m, we can combine the last equality in Eq. (A26) and Eq. (A34) to obtain an implicit relation of $W = W(h)$. Using $V \leq 1$, it is then straightforward to show that $dW/dh > 0$, and hence $W = W_m$ when h is minimized. Given that $h \geq 1$, we therefore have

$$W_m = \frac{\sqrt{\tilde{S}_m^2 + \rho_*^2}}{\sqrt{\gamma}}. \quad \text{(A41)}$$

This equation can be combined with Eq. (A37), resulting in a quartic equation for W_m:

$$(\gamma W_m^2 - \rho_*^2)(W_m + \bar{B}^2)^2 - W_m^2 \tilde{S}^2 - (\bar{B}^i \tilde{S}_i)^2 (\bar{B}^2 + 2W_m) = 0,$$

which may be solved analytically. Alternatively, Eqs. (A37) and (A41) may be solved using an iterative scheme. We start by using Eq. (A32) and choose an initial guess $W_m = [(\hat{\bar{B}}^i \tilde{S}_i)^2 + \rho_*^2]^{1/2}/\sqrt{\gamma}$. Next we compute the initial guess $\tilde{S}_m^2$ using Eq. (A37). We then recompute W_m using Eq. (A41) and $\tilde{S}_m^2$ using Eq. (A37). We keep iterating until the values of $\tilde{S}_m^2$ and W_m converge.

In the previous subsection, we proved that in the absence of magnetic fields $\rho_* \geq 0$, $\tilde{\tau} \geq 0$ and $\tilde{S}^2 \leq \tilde{\tau}(\tilde{\tau} + 2\rho_*)$ are the necessary and sufficient conditions for the inversion to produce the primitive variables in the physical range for the Γ-law EOS with $1 < \Gamma \leq 2$. In the presence of magnetic fields, the necessary and sufficient conditions for the Γ-law EOS with $1 < \Gamma \leq 2$ are replaced by the following inequalities:

$$\rho_* \geq 0, \quad \text{(A42)}$$

$$\tilde{\tau}_{\rm fluid} \geq 0, \quad \text{(A43)}$$

$$\tilde{\tau}_{\rm fluid}(\tilde{\tau}_{\rm fluid} + 2\rho_*) \geq \tilde{S}^2_{\rm fluid}. \quad \text{(A44)}$$

Unfortunately, no simple, analytic expression for necessary and sufficient conditions between the conservatives ρ_*, $\tilde{S}_i$, $\tilde{\tau}$ seems to exist in the presence of magnetic fields. However, necessary and sufficient conditions can be derived separately by combining Eqs. (A42)–(A44), (A36) and (A39). The results are as follows.

Necessary conditions for guaranteeing a physical solution:

$$\rho_* \geq 0, \quad \text{(A45)}$$

$$\tilde{\tau} \geq \frac{\sqrt{\gamma}}{2}\bar{B}^2, \quad \text{(A46)}$$

$$\tilde{S}_m^2 \leq \left(\tilde{\tau} - \frac{\sqrt{\gamma}}{2}\bar{B}^2\right)\left(\tilde{\tau} - \frac{\sqrt{\gamma}}{2}\bar{B}^2 + 2\rho_*\right). \quad \text{(A47)}$$

Sufficient conditions for guaranteeing a physical solution:

$$\rho_* \geq 0, \quad \text{(A48)}$$

$$\tilde{\tau}_m \geq 0, \quad \text{(A49)}$$

$$\tilde{\tau}_m(\tilde{\tau}_m + 2\rho_*) \geq \tilde{S}^2. \quad \text{(A50)}$$

Both $\tilde{S}_m^2$ and $\tilde{\tau}_m$ are nonlinear functions of ρ_*, $\tilde{S}_i$, and $\tilde{\tau}$. Unlike the pure hydrodynamic case, these inequalities are not trivial to impose strictly, so they are imposed approximately as follows. First, a parameter $\psi^6_{\rm thr}$ is introduced, which determines whether the region under consideration is deep inside the BH horizon. For regions deep inside the BH horizon, defined by $\sqrt{\gamma} = \psi^6 \geq \psi^6_{\rm thr}$, the primary goal is to keep the evolution stable and prevent inaccurate data from leaking out of the BH horizon. We find that imposing the sufficient conditions (A48)–(A50) approximately in this region is adequate (detailed recipe below). In regions where $\psi^6 \leq \psi^6_{\rm thr}$, the goal is to evolve the GRMHD equations as accurately as possible, which means that imposing the sufficient conditions is not appropriate. We instead impose two of the necessary conditions (A45) and (A46) only. Since we do not strictly impose all the inequalities, inversion failures sometimes occur. Failures are fixed by replacing the $\tilde{\tau}$ equation by the equation $P = P_{\rm cold}(\rho_0)$. We will demonstrate in Sec. A 4 that the set of equations $\rho_* = \gamma_v \sqrt{\gamma}\,\rho_0$, Eq. (A24) and $P = P_{\rm cold}(\rho_0)$ always results in the primitive variables in the physical range. Our detailed recipe is described in the following subsection.

3. Algorithm for Imposing MHD/Hydrodynamic Inequalities

1. In any region, if $\rho_* \leq 0$, set $\rho_0 = \rho_{\rm atm}$, $P = P_{\rm atm}$, $u_i = 0$ and recompute the conservative variables. If $\tilde{\tau} \leq \sqrt{\gamma}\,\bar{B}^2/2$, reset $\tilde{\tau} = \tilde{\tau}_{\rm atm} + \sqrt{\gamma}\,\bar{B}^2/2$.

2. In the region where $B^i = 0$, if $\tilde{\tau} \leq 0$, reset $\tilde{\tau} = \tilde{\tau}_{\rm atm}$. If $\tilde{S}^2 > \tilde{\tau}(\tilde{\tau} + 2\rho_*)$, replace

$$\tilde{S}_i \to \tilde{S}_i \sqrt{\frac{\tilde{\tau}(\tilde{\tau} + 2\rho_*)}{\tilde{S}^2}}. \quad \text{(A51)}$$

3. In the region where $\psi^6 \geq \psi^6_{\rm thr}$ (deep inside the BH horizon): First, estimate W_m and S_m^2 as follows

$$W_{m0} = \psi^{-6}\left[(\hat{\bar{B}}^i \tilde{S}_i)^2 + \rho_*^2\right]^{1/2}, \quad \text{(A52)}$$

$$\tilde{S}^2_{m0} = \frac{W_{m0}^2 \tilde{S}^2 + (\hat{\bar{B}}^i \tilde{S}_i)^2 (\bar{B}^2 + 2W_{m0})}{(W_{m0} + \bar{B}^2)^2}, \quad \text{(A53)}$$

$$W_m = \psi^{-6}\left(\tilde{S}^2_{m0} + \rho_*^2\right)^{1/2}. \quad \text{(A54)}$$

Next, calculate S_m and $\tilde{\tau}_m$ from Eqs. (A37) and (A40). Then check if $\tilde{\tau}_m \geq \tilde{\tau}_{\rm atm}$. If $\tilde{\tau}_m < \tau_{\rm atm}$ reset $\tilde{\tau}$ (without changing W_m and $\tilde{S}_i$) according to

$$\tilde{\tau} = \tilde{\tau}_{\rm atm} + \frac{\sqrt{\gamma}}{2}\bar{B}^2 + \frac{\bar{B}^2 \tilde{S}^2 - (\bar{B}^i \tilde{S}_i)^2}{2\sqrt{\gamma}\,(W_m + \bar{B}^2)^2}. \quad \text{(A55)}$$

Then check if $\tilde{S}^2 \leq \tilde{\tau}_m(\tilde{\tau}_m + 2\rho_*)$. If not, reset $\tilde{S}_i$ (without changing $\tilde{\tau}_m$ and ρ_*) according to

$$\tilde{S}_i \to \tilde{S}_i \sqrt{\frac{\tilde{\tau}_m(\tilde{\tau}_m + 2\rho_*)}{\tilde{S}^2}}. \quad \text{(A56)}$$

These procedures do not strictly impose the sufficient conditions (A49) and (A50), but can significantly reduce inversion failures.

4. If the inversion still fails after going through all the above steps, replace the $\tilde{\tau}$ equation (A25) by $P = P_{\rm cold}(\rho_0)$ and perform the inversion. This procedure guarantees to produce the primitive variables in the physical range, as will be shown in the next subsection.

4. Inversion using ρ_*, $\tilde{S}_i$ and $P = P_{\rm cold}(\rho_0)$

After imposing the conservative variables inequalities as described in the previous subsection, sometimes the conservatives→primitives variable inversion still fails. In this case, an alternative inversion is imposed, solving for ρ_0 and u_i from the equations $\rho_* = \sqrt{\gamma}\,\gamma_v\rho_0$, $P = P_{\rm cold}(\rho_0)$ and Eq. (A24). We will prove that this inversion always results in the primitive variables in the physical range.

First consider the case $B^i = 0$ for the Γ-law EOS with $1 < \Gamma \leq 2$. In this case, simple, analytic expressions for the necessary and sufficient conditions exist, are easy to implement (as described in Secs. A 1 & A 3), and guarantee successful inversions. However, since the analysis is much simpler than the general case, it is instructive to study the alternative inversion scheme for this case first. It follows from $\rho_* = \sqrt{\gamma}\,\gamma_v\rho_0$, $P = P_{\rm cold}(\rho_0)$ and Eq. (A9) that

$$\rho_0 = \frac{\rho_*}{\sqrt{\gamma}}\left[1 + \frac{\tilde{S}^2}{\rho_*^2 h_{\rm cold}^2(\rho_0)}\right]^{-1/2}, \qquad \text{(A57)}$$

where $h_{\rm cold} = 1 + \epsilon_{\rm cold}(\rho_0) + P_{\rm cold}(\rho_0)/\rho_0$ is the specific enthalpy for the cold EOS. The above equation is an implicit equation for ρ_0. Define the function

$$f(\rho_0) = \rho_0 - \frac{\rho_*}{\sqrt{\gamma}}\left[1 + \frac{\tilde{S}^2}{\rho_*^2 h_{\rm cold}^2(\rho_0)}\right]^{-1/2}. \qquad \text{(A58)}$$

and introduce two variables

$$\rho_1 \equiv \frac{\rho_*}{\sqrt{\gamma}}\left(1 + \frac{\tilde{S}^2}{\rho_*^2}\right)^{-1/2} \quad , \quad \rho_2 \equiv \frac{\rho_*}{\sqrt{\gamma}}. \qquad \text{(A59)}$$

Since $h_{\rm cold} \geq 1$, for given values of $\rho_* > 0$ and $\tilde{S}_i \in (-\infty, \infty)$, $f(\rho_1) \leq 0$ and $f(\rho_2) \geq 0$. Hence there exists $\rho_0 \in [\rho_1, \rho_2]$ that satisfies Eq. (A57) provided that $h_{\rm cold}(\rho_0)$ is continuous in $[\rho_1, \rho_2]$, which is true for the Γ-law EOS. This proves that the inversion always produces ρ_0, as well as P in the physical range. The value of γ_v is then given by $\gamma_v = \rho_*/(\sqrt{\gamma}\,\rho_0)$. For $\rho_0 \in [\rho_1, \rho_2]$, we have $1 \leq \gamma_v \leq \sqrt{1 + \tilde{S}^2/\rho_*^2}$, which is also in the physical range. Finally, the velocity v^i is recovered from Eqs. (A22) and (A23).

Next consider the case $B^i \neq 0$. Equations (A26) and (A34) yield

$$W = \frac{\sqrt{\tilde{S}^2_{\rm fluid} + (\rho_* h_{\rm cold})^2}}{\sqrt{\gamma}}, \qquad \text{(A60)}$$

$$\tilde{S}^2_{\rm fluid} = \frac{W^2\tilde{S}^2 + (\bar{B}^i\tilde{S}_i)^2(\bar{B}^2 + 2W)}{(W + \bar{B}^2)^2}, \qquad \text{(A61)}$$

$$\rho_0 = \frac{\rho_*}{\sqrt{\gamma}}\left[1 + \frac{\tilde{S}^2_{\rm fluid}}{\rho_*^2 h_{\rm cold}^2(\rho_0)}\right]^{-1/2}, \qquad \text{(A62)}$$

where $\tilde{S}^2_{\rm fluid}$ is regarded as an implicit function of $\tilde{S}_i$, $\bar{B}^i$, ρ_* and ρ_0 through Eqs. (A60) and (A61). Hence Eq. (A62) is an implicit equation for ρ_0. Next define

$$f(\rho_0) = \rho_0 - \frac{\rho_*}{\sqrt{\gamma}}\left[1 + \frac{\tilde{S}^2_{\rm fluid}}{\rho_*^2 h_{\rm cold}^2(\rho_0)}\right]^{-1/2}, \qquad \text{(A63)}$$

where ρ_1 and ρ_2 are as in Eq. (A59). Section A 3 proved that $(\hat{\bar{B}}^i\tilde{S}_i)^2 \leq \tilde{S}^2_{\rm fluid} \leq \tilde{S}^2$ [Eqs. (A32) and (A36)]. It follows that $f(\rho_1) \leq 0$ and $f(\rho_2) \geq 0$. Hence a solution exists for $\rho_0 \in [\rho_1, \rho_2]$ as in the pure hydro case, provided that both $h_{\rm cold}(\rho_0)$ and $\tilde{S}^2_{\rm fluid}(\rho_0)$ are continuous in $[\rho_1, \rho_2]$. The inversion thus produces ρ_0 as well as P and γ_v in the physical range. Applying some algebraic manipulations to Eqs. (A24) and (3), we recover the 4-velocity using the formula (c.f. Eq. (31) of [87])

$$u_i = \left[\tilde{S}_i + \frac{\sqrt{\gamma}\,(\bar{B}^j\tilde{S}_j)}{\gamma_v\rho_* h_{\rm cold}(\rho_0)}\bar{B}_i\right]\left[\rho_* h_{\rm cold}(\rho_0) + \frac{\sqrt{\gamma}\,\bar{B}^2}{\gamma_v}\right]^{-1}$$

and the 3-velocity v^i from Eq. (A23).

In conclusion, when using the equations $\rho_* = \sqrt{\gamma}\,\gamma_v\rho_0$, $P = P_{\rm cold}(\rho_0)$ and Eq. (A24), the inversion will always produce the primitive variables in the physical range for any $\rho_* > 0$ and $\tilde{S}_i \in (-\infty, \infty)$.

[1] B. Abbott and the LIGO Scientific Collaboration, Phys. Rev. D **77**, 062002 (Mar. 2008).

[2] D. A. Brown, S. Babak, P. R. Brady, N. Christensen, T. Cokelaer, J. D. E. Creighton, S. Fairhurst, G. Gonzalez, E. Messaritaki, B. S. Sathyaprakash, P. Shawhan, and N. Zotov, Class. Quant. Grav. **21**, S1625 (Oct.

2004).
[3] F. Acernese and the VIRGO Collaboration, Class. Quant. Grav. **23**, S635 (Oct. 2006).
[4] F. Beauville and the LIGO-VIRGO Working Group, Classical and Quantum Gravity **25**, 045001 (Feb. 2008).
[5] H. Lück and the GEO600 collaboration, Class. Quant. Grav. **23**, S71 (Apr. 2006).
[6] K. Kuroda and LCGT Collaboration, Classical and Quantum Gravity **27**, 084004 (Apr. 2010).
[7] `http://www.gravity.uwa.edu.au/docs/aigo_prospectus.pdf`.
[8] G. Heinzel, C. Braxmaier, K. Danzmann, P. Gath, J. Hough, O. Jennrich, U. Johann, A. Rüdiger, M. Sallusti, and H. Schulte, Class. Quant. Grav. **23**, S119 (Apr. 2006).
[9] S. Kawamura and the DECIGO collaboration, Class. Quant. Grav. **23**, S125 (Apr. 2006).
[10] B. Sathyaprakash *et al.*, "Scientific Potential of Einstein Telescope," (Aug. 2011), arXiv:1108.1423 [gr-qc].
[11] S. Hild *et al.*, Classical and Quantum Gravity **28**, 094013 (May 2011).
[12] M. D. Duez, Y. T. Liu, S. L. Shapiro, M. Shibata, and B. C. Stephens, in Proceedings of the Eleventh Marcel Grossmann Meeting on General Relativity, ed. H. Kleinert, R. T. Jantzen, and R. Ruffini (World Scientific, Singapore, 2007).
[13] B. C. Stephens, M. D. Duez, Y. T. Liu, S. L. Shapiro, and M. Shibata, in Proceedings of the Eleventh Marcel Grossmann Meeting on General Relativity, ed. H. Kleinert, R. T. Jantzen, and R. Ruffini (World Scientific, Singapore, 2007).
[14] M. Shibata, Y. T. Liu, S. L. Shapiro, and B. C. Stephens, Phys. Rev. D **74**, 104026 (Nov. 2006).
[15] M. Shibata, K. Taniguchi, and K. Uryū, Phys. Rev. D **68**, 084020 (Oct. 2003).
[16] M. Shibata, K. Taniguchi, and K. Uryū, Phys. Rev. D **71**, 084021 (Apr. 2005).
[17] M. Shibata and K. Taniguchi, Phys. Rev. D **73**, 064027 (Mar. 2006).
[18] M. Shibata, Y. Sekiguchi, and R. Takahashi, Prog. Theor. Phys. **118**, 257 (Aug. 2007).
[19] L. Baiotti, B. Giacomazzo, and L. Rezzolla, Phys. Rev. D **78**, 084033 (Oct. 2008), arXiv:0804.0594 [gr-qc].
[20] J. A. Faber, T. W. Baumgarte, S. L. Shapiro, K. Taniguchi, and F. A. Rasio, Phys. Rev. D **73**, 024012 (Jan. 2006).
[21] J. A. Faber, T. W. Baumgarte, S. L. Shapiro, and K. Taniguchi, Astrophys. J.Lett. **641**, L93 (Apr. 2006).
[22] M. Shibata and K. Uryū, Phys. Rev. D **74**, 121503(R) (Dec. 2006).
[23] M. Shibata and K. Uryū, Class. Quant. Grav. **24**, S125 (Jun. 2007).
[24] M. Shibata and K. Taniguchi, Phys. Rev. D **77**, 084015 (Apr. 2008).
[25] Z. B. Etienne, J. A. Faber, Y. T. Liu, S. L. Shapiro, K. Taniguchi, and T. W. Baumgarte, Phys. Rev. D **77**, 084002 (Apr. 2008).
[26] Z. B. Etienne, Y. T. Liu, S. L. Shapiro, and T. W. Baumgarte, Phys. Rev. D **79**, 044024 (Feb. 2009).
[27] N. Gehrels, J. K. Cannizzo, and J. P. Norris, New Journal of Physics **9**, 37 (Feb. 2007).
[28] V. Kalogera, K. Belczynski, C. Kim, R. O'Shaughnessy, and B. Willems, Phys. Rept. **442**, 75 (Apr. 2007).
[29] J. Abadie, B. P. Abbott, R. Abbott, M. Abernathy, T. Accadia, F. Acernese, C. Adams, R. Adhikari, P. Ajith, B. Allen, and et al., Classical and Quantum Gravity **27**, 173001 (Sep. 2010).
[30] W. H. Lee, Mon. Not. R. Astron. Soc. **328**, 583 (Dec. 2001).
[31] S. Rosswog, R. Speith, and G. A. Wynn, Mon. Not. R. Astron. Soc. **351**, 1121 (Jul. 2004).
[32] S. Rosswog, Astrophys. J. **634**, 1202 (Dec. 2005).
[33] S. Kobayashi, P. Laguna, E. S. Phinney, and P. Mészáros, Astrophys. J. **615**, 855 (Nov. 2004).
[34] E. Rantsiou, S. Kobayashi, P. Laguna, and F. A. Rasio, Astrophys. J. **680**, 1326 (Jun. 2008).
[35] F. Löffler, L. Rezzolla, and M. Ansorg, Phys. Rev. D **74**, 104018 (Nov. 2006).
[36] T. Yamamoto, M. Shibata, and K. Taniguchi, Phys. Rev. D **78**, 064054 (Sep. 2008).
[37] M. Shibata, K. Kyutoku, T. Yamamoto, and K. Taniguchi, Phys. Rev. D **79**, 044030 (Feb. 2009).
[38] K. Kyutoku, M. Shibata, and K. Taniguchi, Phys. Rev. D **82**, 044049 (Aug. 2010).
[39] M. D. Duez, F. Foucart, L. E. Kidder, H. P. Pfeiffer, M. A. Scheel, and S. A. Teukolsky, Phys. Rev. D **78**, 104015 (Nov. 2008).
[40] M. D. Duez, F. Foucart, L. E. Kidder, C. D. Ott, and S. A. Teukolsky, Classical and Quantum Gravity **27**, 114106 (Jun. 2010).
[41] F. Foucart, M. D. Duez, L. E. Kidder, and S. A. Teukolsky, Phys. Rev. D **83**, 024005 (Jan. 2011).
[42] S. Chawla, M. Anderson, M. Besselman, L. Lehner, S. L. Liebling, P. M. Motl, and D. Neilsen, Physical Review Letters **105**, 111101 (Sep. 2010).
[43] B. C. Stephens, W. E. East, and F. Pretorius, ArXiv e-prints(May 2011), arXiv:1105.3175 [astro-ph.HE].
[44] W. E. East, F. Pretorius, and B. C. Stephens, ArXiv e-prints(Nov. 2011), arXiv:1111.3055 [astro-ph.HE].
[45] K. Kyutoku, H. Okawa, M. Shibata, and K. Taniguchi, ArXiv e-prints(Aug. 2011), arXiv:1108.1189 [astro-ph.HE].
[46] M. Shibata and K. Taniguchi, Living Reviews in Relativity **14**, 6 (Aug. 2011).
[47] F. Foucart, M. D. Duez, L. E. Kidder, M. A. Scheel, B. Szilagyi, and S. A. Teukolsky, ArXiv e-prints(Nov. 2011), arXiv:1111.1677 [gr-qc].
[48] T. W. Baumgarte, M. L. Skoge, and S. L. Shapiro, Phys. Rev. D **70**, 064040 (Sep. 2004).
[49] K. Taniguchi, T. W. Baumgarte, J. A. Faber, and S. L. Shapiro, Phys. Rev. D **72**, 044008 (Aug. 2005).
[50] K. Taniguchi, T. W. Baumgarte, J. A. Faber, and S. L. Shapiro, Phys. Rev. D **74**, 041502 (Aug. 2006).
[51] K. Taniguchi, T. W. Baumgarte, J. A. Faber, and S. L. Shapiro, Phys. Rev. D **75**, 084005 (Apr. 2007).
[52] K. Taniguchi, T. W. Baumgarte, J. A. Faber, and S. L. Shapiro, Phys. Rev. D **77**, 044003 (Feb. 2008).
[53] N. Vlahakis and A. Königl, Astrophys. J. **596**, 1080 (Oct. 2003).
[54] N. Vlahakis and A. Königl, Astrophys. J. **596**, 1104 (Oct. 2003).
[55] T. Piran, Reviews of Modern Physics **76**, 1143 (Jan. 2005).
[56] However, it has been suggested that during the BHNS inspiral the interaction of BH and NS magnetic fields could drive a Poynting flux, which might give rise to observable electromagnetic signals [107].
[57] K. Ioka and K. Taniguchi, Astrophys. J. **537**, 327 (Jul.

2000), arXiv:astro-ph/0001218.
[58] M. Vasúth, Z. Keresztes, A. Mihály, and L. Á. Gergely, Phys. Rev. D **68**, 124006 (Dec. 2003), arXiv:gr-qc/0308051.
[59] B. Mikóczi, M. Vasúth, and L. Á. Gergely, Phys. Rev. D **71**, 124043 (Jun. 2005), arXiv:astro-ph/0504538.
[60] B. Giacomazzo, L. Rezzolla, and L. Baiotti, Mon. Not. Roy. Astron. Soc. **399**, L164 (Oct. 2009), arXiv:0901.2722 [gr-qc].
[61] L. Rezzolla, B. Giacomazzo, L. Baiotti, J. Granot, C. Kouveliotou, and M. A. Aloy, Astrophys. J. Lett. **732**, L6 (May 2011), arXiv:1101.4298 [astro-ph.HE].
[62] Z. B. Etienne, Y. T. Liu, and S. L. Shapiro, Phys. Rev. D **82**, 084031 (Oct. 2010).
[63] Z. B. Etienne, V. Paschalidis, Y. T. Liu, and S. L. Shapiro, ArXiv e-prints(Oct. 2011), arXiv:1110.4633 [astro-ph.HE].
[64] M. Shibata and T. Nakamura, Phys. Rev. D **52**, 5428 (Nov. 1995).
[65] T. W. Baumgarte and S. L. Shapiro, Phys. Rev. D **59**, 024007 (Jan. 1998).
[66] J. R. van Meter, J. G. Baker, M. Koppitz, and D.-I. Choi, Phys. Rev. D **73**, 124011 (Jun. 2006).
[67] T. W. Baumgarte and S. L. Shapiro, *Numerical Relativity: Solving Einstein's Equations on the Computer* (Cambridge University Press, 2010).
[68] T. W. Baumgarte and S. L. Shapiro, Astrophys. J. **585**, 921 (Mar. 2003).
[69] G. B. Cook and H. P. Pfeiffer, Phys. Rev. D **70**, 104016 (Nov. 2004).
[70] `http://www.lorene.obspm.fr/`.
[71] Z. B. Etienne, J. A. Faber, Y. T. Liu, S. L. Shapiro, and T. W. Baumgarte, Phys. Rev. D **76**, 101503(R) (Nov. 2007).
[72] D. Brown, O. Sarbach, E. Schnetter, M. Tiglio, P. Diener, I. Hawke, and D. Pollney, Phys. Rev. D **76**, 081503 (Oct. 2007).
[73] D. Brown, P. Diener, O. Sarbach, E. Schnetter, and M. Tiglio, Phys. Rev. D **79**, 044023 (Feb. 2009).
[74] J.-P. De Villiers, J. F. Hawley, and J. H. Krolik, Astrophys. J. **599**, 1238 (Dec. 2003).
[75] J. C. McKinney and C. F. Gammie, Astrophys. J. **611**, 977 (Aug. 2004).
[76] M. Anderson, E. W. Hirschmann, L. Lehner, S. L. Liebling, P. M. Motl, D. Neilsen, C. Palenzuela, and J. E. Tohline, Phys. Rev. Lett. **100**, 191101 (May 2008).
[77] B. Giacomazzo, L. Rezzolla, and L. Baiotti, Phys. Rev. D **83**, 044014 (Feb 2011).
[78] Y. T. Liu, S. L. Shapiro, Z. B. Etienne, and K. Taniguchi, Phys. Rev. D **78**, 024012 (Jul. 2008).
[79] G. B. Cook, S. L. Shapiro, and S. A. Teukolsky, Astrophys. J. **398**, 203 (Oct. 1992).
[80] `http://www.cactuscode.org/`.
[81] E. Schnetter, S. H. Hawley, and I. Hawke, Class. Quantum Grav. **21**, 1465 (2004), arXiv:gr-qc/0310042, `http://arxiv.org/abs/gr-qc/0310042`.
[82] J. Thornburg, Class. Quant. Grav. **21**, 743 (Jan. 2004).
[83] M. D. Duez, Y. T. Liu, S. L. Shapiro, and B. C. Stephens, Phys. Rev. D **72**, 024028 (Jul. 2005).
[84] P. Colella and P. R. Woodward, Journal of Computational Physics **54**, 174 (Sep. 1984).
[85] A. Harten, P. Lax, and B. van Leer, SIAM Rev. **25**, 35 (1983).
[86] C. R. Evans and J. F. Hawley, Astrophys. J. **332**, 659 (Sep. 1988).
[87] S. C. Noble, C. F. Gammie, J. C. McKinney, and L. Del Zanna, Astrophys. J. **641**, 626 (Apr. 2006).
[88] S. C. Noble, C. F. Gammie, J. C. McKinney, and L. Del Zanna(2006), publicly available on http://rainman.astro.illinois.edu/codelib/.
[89] K. Beckwith and J. M. Stone, Astrophys. J. Supp. **193**, 6 (Mar. 2011).
[90] A. Ashtekar and B. Krishnan, Living Reviews in Relativity **7**, 10 (Dec. 2004).
[91] O. Dreyer, B. Krishnan, D. Shoemaker, and E. Schnetter, Phys. Rev. D **67**, 024018 (Jan. 2003).
[92] M. Boyle and A. H. Mroué, Phys. Rev. D **80**, 124045 (Dec. 2009).
[93] C. Reisswig and D. Pollney, ArXiv e-prints(Jun. 2010), arXiv:1006.1632 [gr-qc].
[94] M. Ruiz, M. Alcubierre, D. Núñez, and R. Takahashi, General Relativity and Gravitation **40**, 1705 (Aug. 2008).
[95] J. H. Krolik and J. F. Hawley, Astrophys. J. **573**, 754 (Jul. 2002), arXiv:astro-ph/0203289.
[96] K. Beckwith, J. F. Hawley, and J. H. Krolik, Mon. Not. Roy. Astron. Soc. **390**, 21 (Oct. 2008), arXiv:0801.2974.
[97] L. Santamaría, F. Ohme, P. Ajith, B. Brügmann, N. Dorband, M. Hannam, S. Husa, P. Mösta, D. Pollney, C. Reisswig, E. L. Robinson, J. Seiler, and B. Krishnan, Phys. Rev. D **82**, 064016 (Sep. 2010).
[98] LIGO Document T0900288-v3 on https://dcc.ligo.org/cgi-bin/DocDB/ShowDocument?docid=2974.
[99] P. Ajith, M. Boyle, D. A. Brown, S. Fairhurst, M. Hannam, I. Hinder, S. Husa, B. Krishnan, R. A. Mercer, F. Ohme, C. D. Ott, J. S. Read, L. Santamaria, and J. T. Whelan, ArXiv e-prints(Sep. 2007), arXiv:0709.0093 [gr-qc].
[100] P. Ajith, M. Hannam, S. Husa, Y. Chen, B. Brügmann, N. Dorband, D. Müller, F. Ohme, D. Pollney, C. Reisswig, L. Santamaría, and J. Seiler, Physical Review Letters **106**, 241101 (Jun. 2011).
[101] J. Miller, Physics Today, 11(Nov. 2011).
[102] B. D. Lackey, K. Kyutoku, M. Shibata, P. R. Brady, and J. L. Friedman, ArXiv e-prints(Sep. 2011), arXiv:1109.3402 [astro-ph.HE].
[103] P. Marronetti, W. Tichy, B. Brügmann, J. González, and U. Sperhake, Phys. Rev. D **77**, 064010 (Mar. 2008).
[104] B. Zink, N. Stergioulas, I. Hawke, C. D. Ott, E. Schnetter, and E. Müller, Phys. Rev. D **76**, 024019 (Jul. 2007), arXiv:astro-ph/0611601.
[105] P. D. Lasky, B. Zink, K. D. Kokkotas, and K. Glampedakis, Astrophys. J. Lett. **735**, L20 (Jul. 2011), arXiv:1105.1895 [astro-ph.SR].
[106] R. Ciolfi, S. K. Lander, G. M. Manca, and L. Rezzolla, Astrophys. J. Lett. **736**, L6 (Jul. 2011), arXiv:1105.3971 [gr-qc].
[107] S. T. McWilliams and J. Levin, ArXiv e-prints(Jan. 2011), arXiv:1101.1969 [astro-ph.HE].